Journal of Energy Storage 72 (2023) 108185

Contents lists available at ScienceDirect

Journal of Energy Storage

journal homepage: www.elsevier.com/locate/est

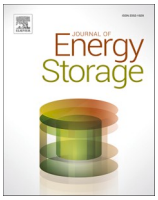

Research papers

Improving the thermal response flexibility of 2- and 3-phase composite phase change materials by metallic triply periodic minimal surface structures

Matteo Molteni *, Sara Candidori, Serena Graziosi, Elisabetta Gariboldi

Politecnico di Milano, Department of Mechanical Engineering, Via La Masa 1, 20156 Milan, Italy

ARTICLE INFO

Keywords:
Composite phase change materials (PCM)
Triply periodic minimal surface
Energy storage
Additive manufacturing

ABSTRACT

The percolation of organic Phase Change Materials (PCMs) into metallic skeletons produces Composite PCMs (C-PCMs). This paper explores Al-Si-Mg alloy Sheet-based Primitive-Schwarz (PS) Triply Periodic Minimal Surface (TPMS) C-PCMs filled by paraffines, comparing them with C-PCMs built with inverse Body-Centred Cubic (BCC) structures. The aim is to derive guidelines for improving the thermal response flexibility of these systems. The lattice geometrical features and C-PCM properties are calculated and modelled as a function of porosity (ε), proportional to storable energy. For $\varepsilon > 0.8$, the Effective Thermal Conductivity (λ_{eff}) of PS-based C-PCMs is higher than that of BCC-based, reaching 68 % of the maximum theoretical value. Design considerations are used to define a set of feasible C-PCMs whose thermal response is numerically simulated. The PS favours shorter transients than BCC (6.3 % less for $\varepsilon = 0.8$). The ε increase, and, consequently, λ_{eff} reduction, in PS-based C-PCMs raises both storage potential and storage times (542 s vs 694 s for $\varepsilon = 0.8$ vs 0.9). Minor changes in the storage times can be obtained by lattice size variation at constant ε. The peculiarity of sheet-based TPMSs of splitting the volume into non-interconnected subdomains is exploited to design 3-phase C-PCMs, employing two PCMs having different melting temperatures.

1. Introduction

In recent years, the scientific community has put a lot of effort into fighting the increasing levels of pollution caused by traditional combustion processes for energy production. The aim is to look for more sustainable solutions able to satisfy, the energy needs of the global population [1–3]. In such a context, Phase Change Materials (PCMs) are gaining more and more attention for Latent Heat Thermal Energy Storage (LHTES) purposes [4–7]. Indeed, their capability of storing thermal energy as latent heat associated with phase changes (i.e., solid-solid, solid-liquid, liquid-gas), and releasing it later with a reverse process, makes PCMs the ideal candidates to efficiently manage the energy of a system. In particular, the high specific and latent heats, combined with easily reachable transition temperatures, make exploiting organic PCMs a promising approach. However, the intrinsic low thermal conductivity limits the performances of LHTES organic-based devices. Different attempts have been made to tackle this issue, creating hybrid composites with organic PCMs having high thermal conductive phases. In this sense, several strategies have been considered in the literature, such as percolating the organic PCM in metal foams [8,9], rather than using carbon skeletons [10–12] or dispersing fillers inside the PCMs [13,14]. The addition of these latter results in a composite PCM (C-PCM) described as a fully homogenised single-phase medium with thermal conductivity (actually, effective thermal conductivity, λ_{eff}) higher than the one of the starting organic phase alone. The thermal conductivity increase depends on the quantity and properties of the second-phase inclusions and how they are arranged in the composite [15]. Different models are proposed in the literature to predict the composite λ_{eff}, highlighting the importance of controlling the morphology and orientation of the second-phase medium to achieve the settled design requirements.

Meanwhile, Additive Manufacturing (AM) technologies, with their unique capabilities to enable the design and fabrication of topologically complex structures [16,17], have pushed the exploration of new design pathways also in this field. Among the topologies already explored to design the so-called architected materials are the Triply Periodic Minimal Surfaces (TPMSs), whose potential in heat transfer, thanks to their

* Corresponding author.
E-mail addresses: matteo1.molteni@polimi.it (M. Molteni), sara.candidori@polimi.it (S. Candidori), serena.graziosi@polimi.it (S. Graziosi), elisabetta.gariboldi@polimi.it (E. Gariboldi).

https://doi.org/10.1016/j.est.2023.108185
Received 21 February 2023; Received in revised form 29 May 2023; Accepted 26 June 2023
Available online 5 July 2023

Nomenclature

Cp	Specific heat at constant pressure, J/kg K^{-1}
f_L	Volumetric average liquid fraction, –
LFR	Liquid fraction rate, 1/s
P	Latent heat storage power, kW m^{-2}
q	Average normal heat flux, W m^{-2}
RT	Room temperature, K
T	Temperature, K
T_m	Melting Temperature, K
tx	Time, s

General terms

AM	Additive manufacturing
C-PCM	Composite Phase Change Material
PCM	Phase Change Material
LHTES	Latent heat thermal energy storage
BCC	Body-centred cubic
PS	Primitive-Schwarz
TPMS	Triply Periodic Minimal Surface

Structures geometrical parameters

Bd	Bottleneck diameter, mm
c	Level-set constant, –
d	Maximum sphere diameter, mm
H	Height of the C-PCM, mm
L	Cell size, mm
N	Number of stacked cells -
R	Normalised surface-to-volume ratio, –
t	PS structure thickness, mm
V	Absolute volume, mm^3
v_s	Volume fraction of the solid, –
S	Contact surface between the metal skeleton and organic PCM, mm^2
S_{face}	Metallic surface on the lateral faces of the bounding box, mm^2
S_{norm}	Contact surface normalised to the surface of the bounding box, mm^2

Greek symbols

α	Thermal diffusivity, m^2/s
ΔH	Latent heat of fusion, J/kg
ΔT	Temperature difference, K
Δtx	Time step, s
Δtx_{melt}	PCM melting time interval, s
$\Delta T/dx$	Average temperature gradient, s
ε	Porosity, –
λ	Thermal conductivity, W m^{-1} K^{-1}
ρ	Density, kg/m^3
η	Microstructural efficiency, –
μ	Morphological index, –

Subscripts

Al	metallic domain of the lattice
PCM	PCM domain of the lattice
eff	effective
$\parallel$	parallel (upper Wiener bound)
$\perp$	Series (lower Wiener bound)
B-A	difference between the reference point B and A
Al-PCM	difference between metallic and PCM phases (volume-averaged)
min	minimum
max	maximum
on	PCM melting onset
off	PCM melting offset

high surface-area-to-volume ratio, has already been investigated [18–23]. TPMSs are characterised by surfaces having zero mean curvature at any point. This feature implies minimising surface energy and area locally [24–26]. That peculiarity makes them particularly attractive for improving thermal and chemical exchange processes such as heat exchange, filtering, bone scaffold regeneration, catalytic converters, fuel cells, and batteries [27–33] thanks to the high surface-to-volume ratio characterising their topology. Several studies have already been conducted to characterise the mechanical [34–41] and the thermal behaviour of TPMS-based structures [18,42–45]. These TPMS-based lattices are periodic cellular structures whose geometry can be modelled through level-set equations expressed as (Eq. (1), [26]):

$$\phi(x,y,z) = c \tag{1}$$

where c is a constant that defines the morphology of the surface, as shown in Fig. 1 (central row). In this figure, the widely investigated Primitive-Schwarz (PS) TPMS (Eq. (2), [22,46,47]) is taken as a reference whose topology can be approximated using the following level-set equation:

$$cos\left(\frac{2\pi}{L_x}x\right) + cos\left(\frac{2\pi}{L_y}y\right) + cos\left(\frac{2\pi}{L_z}z\right) = c \tag{2}$$

where L_x, L_y and L_z are the unit cell sizes in the three principal directions [26]. For a cubic unit cell, a unique L value is considered.

When c equals zero, the TPMS surface splits the space into two not-self-intersecting subdomains [48,49]. By tuning c, the result of this splitting process can be modified as desired. The 3D topologies generated from these surfaces characterised by a given c-value are of two kinds: Sheet- and Solid-network TPMS-based lattices [50]. The formers are created by thickening the surface (Fig. 1, top row). Besides, as it will be clarified in Section 2.1, they can also split the space into three subdomains, one of which can be considered a solid and the other void. For example, this thickening effect can be obtained by modifying the c value. The Solid-based TPMS are instead generated considering one subdomain as fully solid and the other as void (Fig. 1, bottom row). Hence, they split the space into two subdomains. In the case of the Solid-based TPMS, the solid and void volume fractions - this latter coincides with the porosity (i.e., v_S and ε, respectively) - are equal when $c = 0$ (Fig. 1) [22,46,47].

v_S is the ratio between the volume of the unit cell and the volume of its cubic bounding box, while ε is its complement to 1 or 100, if expressed as a fraction or percentage, respectively. The Solid-based TPMSs present a volume fraction threshold value below which the resulting solid is no more continuous. In contrast, the thickness of the walls controls the volume fraction (v_s) in the Sheet-based ones (Fig. 1). This thickness can be varied by modifying the c value.

In this study, Sheet-based lattices are considered because they allow reaching extremely low v_S values for the skeleton phase (i.e., high ε), keeping the continuity of the solid domain [26]. These values are essential to increase the amount of PCM stored in the C-PCM and, consequently, the amount of storable heat. The high surface-to-volume ratio that can be obtained with Sheet-based TPMSs at a low volume fraction of the solid phase (characterised by high thermal conductivity and high strength if metallic), and the possibility to fill the high remaining volume by low-conductivity and low-melting organic PCMs, suggests this type of TPMS structures as interesting candidates for creating PCM-based composites. Their adoption could be added to the widely investigated composites in which PCMs fill the interconnected

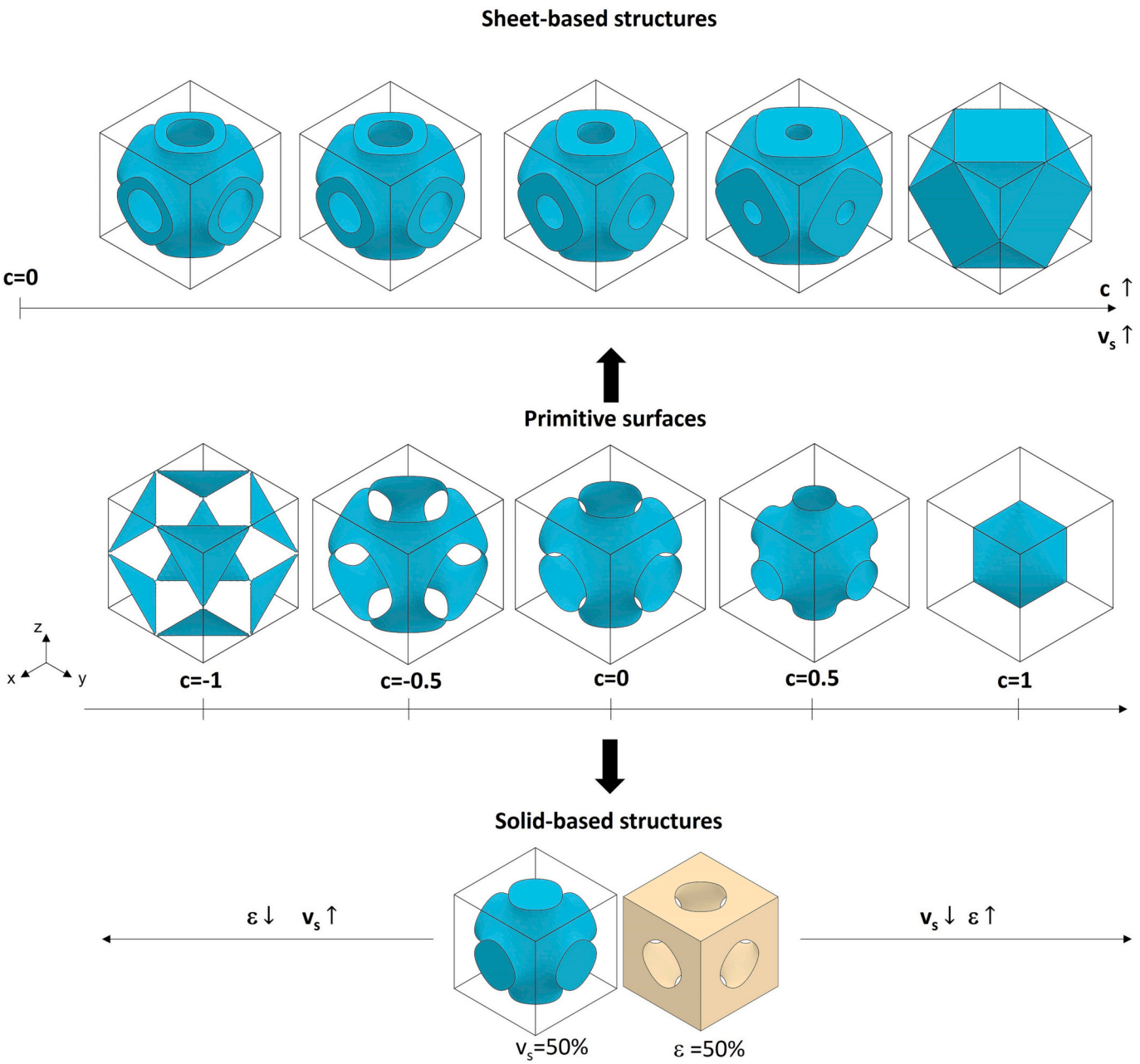

Fig. 1. Design of 3D structures starting from PS surfaces. Central row: modification of the zero-thickness surface by changing the c value (Eq. (2)). Top row: different sheet-based PS structures obtained modifying the c parameter. Higher c values, from left to right, correspond to increased volume fractions (v_s) and thus thickness. Bottom row: Solid-based PS structures obtained by solidifying one of the two subdomains. When c = 0, vs is equal to ε, i.e., 50 %. Equilibrium can be altered by changing the c value.

porosity in foams [51,52] or more conventional lattices (e.g., Body-Centred Cubic, Face-Centred Cubic) [53–57]. Due to this typical production method for composite PCMs, also implementable with TPMS structures, the structure can be characterised either in terms of solid phase or porosity. Notwithstanding this potential, to the authors' knowledge, only a few papers have explored the possibility of combining TPMSs with organic PCMs.

Qureshi et al. recently published a series of studies [58–62] investigating the potentiality of TPMS lattice systems leveraging numerical simulations. Their results show several advantages of TPMSs compared to conventional foams, represented by the well-known Kelvin unit cell. TPMS structures exhibit superior λ_{eff} and heat transfer coefficients compared to the latter. In addition, they offer sensible reductions in the time necessary to completely melt the PCM embedded in the composite. The influence of the choice of the TPMS topology with different levels of porosity, the positive impact of the graded distribution of the solid material inside the PCM, and their introduction in finned devices were considered in these studies. Qureshi et al.'s analyses demonstrated [58] that there are no significant differences in the effective thermal conductivity value when various TPMS morphologies with fixed volume fraction (at least among the investigated PS, Gyroid, and Schoen I-WP TPMSs) are combined with PCM. That study also demonstrated that the Sheet-based PS structure has a slightly higher effective thermal conductivity than the others [58]. Hence, starting from the Sheet-based PS structure as a promising topology, this paper further deepens the thermal behaviour of composite PCMs (C-PCMs). These C-PCMs consists of a Sheet-based PS structure made of Al-Si-Mg alloy (widely processed by AM technologies) combined with paraffins as the active PCM phase. The

paraffines have been selected for their low density, low costs, and easily tunable thermophysical properties [63]. The Al-alloy was chosen for its low cost, low density, recyclability and AM processability. While other high-conductivity materials could be potentially adopted to fabricate the metallic skeletons, the previously listed properties should be considered before replacing an Al-based alloy. For example, at the moment, the use of copper (Cu), commonly adopted for foams [64], is still challenging when there is the need to manufacture small-scale lattices [65].

The contribution of the paper is four-fold. Firstly, analytical models of the main geometrical features of C-PCMs are provided. These models allow supporting the evaluation of the feasibility of the metallic skeletons with the selected AM technology. Second, the study provides an analytical description of the effective thermal conductivity of the investigated C-PCMs in the same porosity range adopted for deriving the previous models. Third, the study also estimates the impact of cell size and porosity within the feasibility limits of AM process on the potentiality of tuning the thermal response of the C-PCMs under simulated service conditions. Fourth, sheet-based TPMSs are exploited to create 3-phase C-PCMs, which have not yet been discussed in the literature. These latter are obtained by filling the two void and non-self-intersecting subdomains generated by sheet-based TPMS with two different PCMs. Two paraffins characterised by different activation temperatures are used. An evaluation of the tuning potential offered by this innovative 3-phase energy storage system is provided.

The paper is organised as follows: Section 2 describes the materials and numerical methods employed for the analysis; Section 3 presents and discusses the obtained results; in Section 4, conclusions are reported. Sections 2 and 3 are subdivided accordingly to the aims of the paper: the description of geometrical features for AM processing of metallic skeleton, the corresponding effective thermal conductivity from steady state analyses, the tuning of C-PCM thermal behaviour during transients, the feasibility of 3-phase C-PCMs with the Sheet-based PS lattice.

2. Materials and methods

The study is grounded on the analyses of the main design parameters of Sheet-based PS and inverse BCC structures and their influence on the thermal behaviour of the C-PCMs. Analytical correlations among these parameters are provided to offer design indications for developing structures with well-defined thermal properties. Then, numerical simulations (both steady-state and transient analyses) are used to investigate the C-PCM thermal response and extrapolate the influence of the design parameters. Steady-state analyses allow evaluating the λ_{eff} of the C-PCM. Transient studies allow for assessing the behaviour of a structure under a specific thermal input, simulating particular working conditions. These analyses are conducted on the basis of the work of Li and Gariboldi for C-PCMs made with an Al BCC lattice and paraffins [66].

An overview of the characteristics of the composite structures analysed in this paper is provided in Table 1. Further details are available in the following sections, while for clarifications concerning the acronyms used, the reader is invited to refer to the list of abbreviations. The analysed structures have been labelled as "*Arch.-L-ε-N*", i.e., "type of architecture"-"cell size"-"porosity"-"number of stacked cells" (in Table 1, "P-10-0.8-1" stands for a structure created using the Sheet-based PS, with a cell size of 10 mm, a porosity of 0.8 and 1 cell). As shown in Tables 1, 3 cases will be analysed for the transient analysis to study the influence on the thermal behaviour of the C-PCM of the following design aspects: 1) the morphology of the metallic phase (i.e., PS vs Inverse BCC, Case 1); 2) the porosity (i.e., ε) selected for the PS structure (Case 2); 3) the cell size chosen for the PS structure (Case 3).

2.1. Size-normalised geometry description of C-PCM structures

The Inverse BCC (from now on called only BCC for simplification) and PS lattices (Fig. 2) can both be produced through the regular repetition of cubic unit cells, which are characterised by a side length or cell size (L) and a volume fraction (v_s) [26]. However, in the case of C-PCMs, v_s is meaningless because the latent heat storage potential is proportional to the volume fraction of the percolated PCM phase, which occupies the "void" domain, from now on referred to as ε. Hence, this latter parameter is the one considered in this study. The MSLattice [50] software was used to generate the PS digital models, while the Inverse BCC was modelled using Autodesk Inventor (www.autodesk.com). The geometrical parameters were extrapolated using both Autodesk Inventor and Rhinoceros (www.rhino3d.com). This latter was also used to obtain the area values of the PS surfaces. The PS was designed by controlling the ε in the range of 0.68–0.99 for $L = 10$ mm and $L = 5$ mm, using the "uniform TPMS lattices" module, "sheet networks" option [50]. The minimum and maximum thickness (t_{max} and t_{min}, respectively), shown in Fig. 2, were measured for each PS cell. Indeed, the resulting thickness of the PS "walls" is not constant. The BCC (Fig. 2) was obtained by performing a series of Boolean operations considering spheres of diameter d located at the vertex of a cube and in its central point. The resulting void domain is fully connected. This cell is among those adopted to describe open-cell foams [67]. The solid structure is continuous and forms interconnected voids in the ε range of 0.68–0.995. The correlations between L, ε and d are described in [55].

Table 1
Geometrical parameters of the Sheet-based PS and BCC structures modelled for the steady-state and transient analyses of the 2-phase C-PCMs. "*" indicates that the data are not available in the ε range considered; "-"means that the parameter is not relevant for that specific structure.

Steady-state analyses (Sections 2.2, 3.2)				
Architecture	Sheet-based PS		Inverse BCC	
Label	P-10-0.68/0.99-1	P-5-0.68/0.99-1	B-10-0.68/0.99-1	B-5-0.68/0.99-1
L [mm]	10	5	10	5
ε [−]	0.68–0.99	0.68–0.99	0.68–0.99	0.68–0.99
t_{min} [mm]	1.477–0.046	0.738–0.099	–	–
Bd [mm]	2.969–4.727	1.484–2.363	*	*
d [mm]	7.629–8.629	3.814–4.315	8.876–10.18	4.438–5.229
H [mm]	10	5	10	5
N [−]	1	1	1	1

Transient analyses (Sections 2.3, 3.3)			
	Case 1 - cell type effect	Case 2 – porosity effect	
Architecture	Inverse BCC	Sheet-based PS	
Label	B-6.67-0.8-3	P-6.67-0.8-3 (ref. C-PCM)	P-6.67-0.9-3
L [mm]	6.67	6.67	6.67
ε [−]	0.8	0.8	0.9
t_{min} [mm]	–	0.616	0.301
Bd [mm]	2.589	2.434	2.813
d [mm]	6.33	5.347	5.562
H [mm]	20	20	20
N [−]	3	3	3

Transient analyses (Sections 2.3, 3.3)				
	Case 3 - cell size effect			
Architecture	Sheet-based PS			
Label	P-6.67-0.8-3	P-5-0.8-4	P-4-0.8-5	P-3.33-0.8-6
L [mm]	6.67	5	4	3.33
ε [−]	0.8	0.8	0.8	0.8
t_{min} [mm]	0.616	0.462	0.369	0.308
Bd [mm]	2.434	1.825	1.460	1.217
d [mm]	5.347	4.008	3.207	2.674
H [mm]	20	20	20	20
N [−]	3	4	5	6

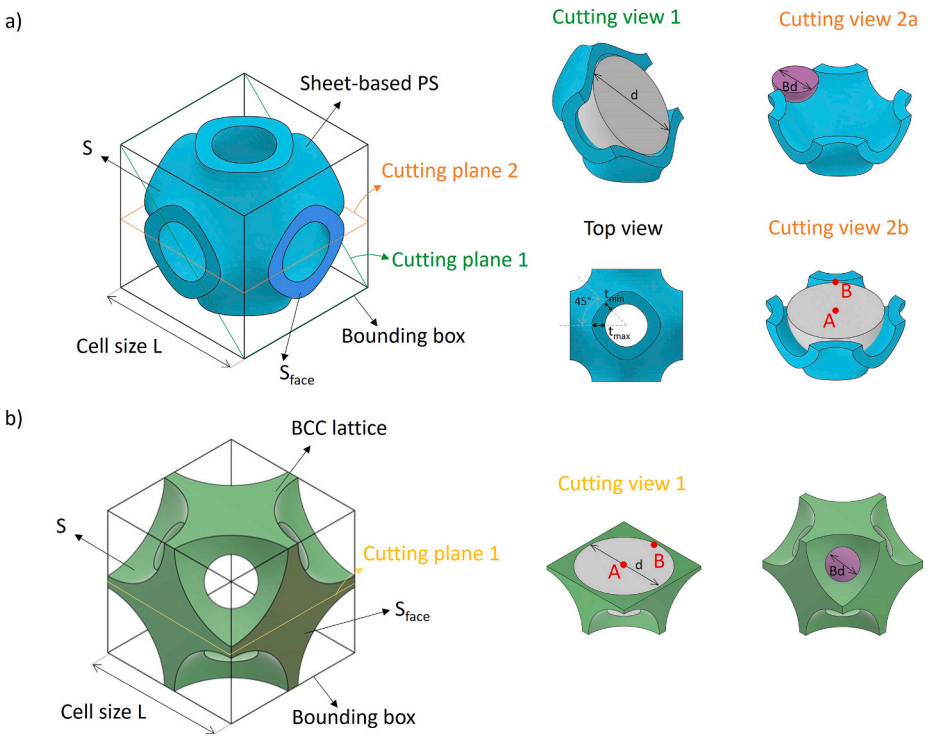

Fig. 2. Main geometrical parameters for the Sheet-based PS (a) and BBC (b) lattices: d is the diameter of the maximum sphere inscribed in the lattice, Bd is the bottleneck diameter, while t_{min} and t_{max} are the minimum and maximum thickness of the sheet-based PS, respectively. S is the contact surface between the metal and the PCM (S_{face} is not considered). The "A" and "B" points on the mid-height plane are used as a reference in Section 3.3: A is at the centre of the sphere of diameter d; B is at the interface between the PCM and the metal domain.

In both cases, the C-PCMs were set up considering the "void" volumes (Fig. 3) occupied by the organic PCM. In the case of PS, these latter can be filled with one or two PCMs, obtaining a 2-phase or a 3-phase C-PCM, respectively (as shown in Fig. 3). Geometry-based indexes, normalised with respect to the lattice size, were chosen for supporting and simplifying the design of C-PCMs. The literature presents some examples of BCC [55] and PS [68–71] but these structures are often described through their relative density (v_s). Surface-to-volume ratios have already been adopted in the literature to describe the thermal responses of lattices [72,73] and TPMS [74]. In this study, two *L*-independent surface-to-volume ratio indexes were calculated not only considering the volume fraction of the metal structure but also the PCM volume. They are referred to as R_{Al} and R_{PCM} and are defined through Eqs. (3) and (4), respectively.

$$R_{Al} = \frac{S/6L^2}{V_{Al}/L^3} = \frac{S_{norm}}{v_s} \tag{3}$$

$$R_{PCM} = \frac{S/6L^2}{V_{PCM}/L^3} = \frac{S_{norm}}{\varepsilon} \tag{4}$$

In Eqs. (3) and (4), *S* [mm^2] refers to the extension of the contact surface between the Al alloy and the PCM (as shown in Fig. 2), while *L* [mm] is the cell size. Hence, S_{norm} refers to the contact surface normalised to the surface of the bounding box for a cubic cell ($6 \cdot L^2$). Only the contact surface between metal and PCM was considered in this calculation. Indeed, the metallic surface laying on the lateral surface of the bounding box (S_{face} in Fig. 2) was neglected since in direct contact with the metal part in the case of a lattice of stacked cells. V_{Al} [mm^3] and v_s are the absolute volume of the metallic lattice and its volume fraction ($v_s = V_{Al}/L^3$), respectively. V_{PCM} [mm^3] corresponds to the void volume filled with the PCM. ε can be thus obtained as V_{PCM}/L^3.

In addition to these *L*-independent indexes, *L*-normalised ratios were also defined for the following geometrical parameters: the maximum diameter (*d* in Fig. 2) of a sphere that can be inscribed inside the unit cell; the minimum and maximum thickness (t_{min} and t_{max} in Fig. 2) of the metal structure; the diameter of the biggest sphere inscribed in the lateral cell side (the bottleneck diameter, *Bd* in Fig. 2). In the BCC lattice, *d* corresponds to the diameter of the sphere used to build the BCC cell, while *Bd* to the minimum diameter created by the intersection of the spheres (Fig. 2). Besides, the thickness was not considered a parameter for this structure because it varies consistently from 0 to an ε-correlated maximum value (further details are provided in Section 3.1). It is worth underlying that the two spheres (represented by *d* and *Bd*) are abstract representations used to make explicit some characteristics of the cell topology. All these geometrical features were also considered for the following reasons. *d*, and the lattice thickness (particularly t_{min}) influence the printability of the metallic skeleton. They should be checked to guarantee that the metal structure is self-supporting. *Bd* influences the filling of the void subdomains of the structure with the PCM. This value also affects how easy-to-clean the metal structure is after the printing, when, for example, the unmelted powder has to be removed. The *d*, t_{min}, t_{max} and *Bd* values for the PS structure were calculated at the *L* and ε values previously mentioned at the beginning of this section. All these parameters, sorted at the design level, were thus selected based on their influence on the printability of the structure. Indeed, considering these Design for Additive Manufacturing (DfAM) aspects since the beginning of the design process of a C-PCM is fundamental to guarantee and monitor its fabricability. As anticipated, these geometrical parameters were *L*-normalised as d/L, Bd/L, t_{max}/L and t_{min}/L. These ratios were used to find their correlation with ε. *L* was selected as the normalising parameter for two main reasons. First, it is the most straightforward design parameter to assign when starting the structure dimensioning, and second, λ_{eff} of the structure does not depend on this value (further details in Section 2.2).

2.2. Effective thermal conductivity calculations for PS and BCC C-PCMs

Numerical simulations were performed with Comsol Multiphysics (version 6.1.) (www.comsol.com) in the stationary state to determine the thermal conductivity of the C-PCM. The whole structure was considered an assembly between the metallic and the organic domains with the creation of identity pairs at their boundaries. All materials composing the C-PCM were considered homogenous in the ε range of

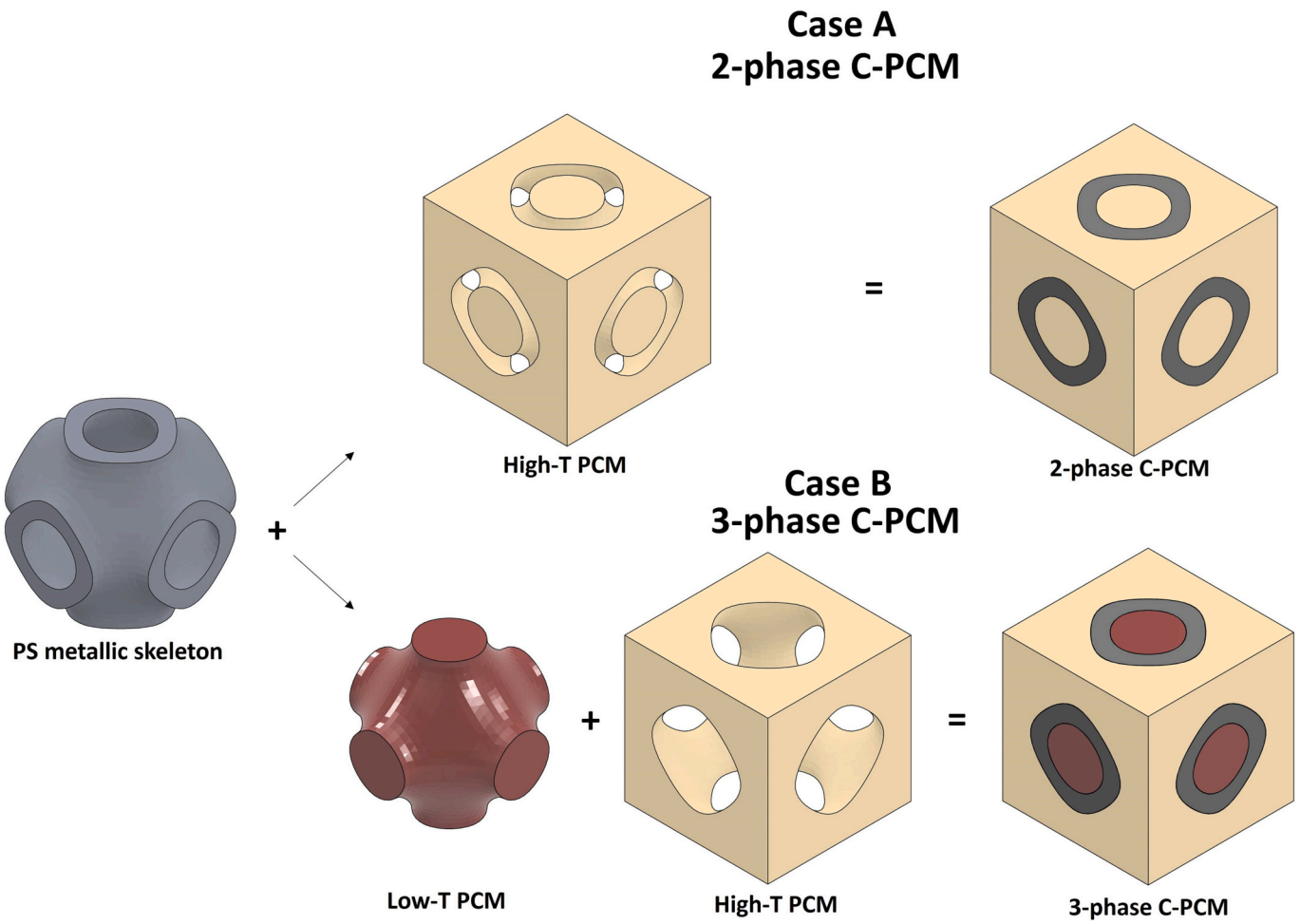

Fig. 3. Schematic view of a single cell of the 2-phase (case "A") and 3-phase (case "B") PS-based C-PCM. The beige and dark red colours refer to high-T PCM and low-T PCM, respectively, while the grey colour to the metallic skeleton. (For interpretation of the references to colour in this figure legend, the reader is referred to the web version of this article.)

0.68–0.99 (Table 1). A quadratic Lagrange discretization was considered for the calculations. The software automatically meshed the structure with a physics-controlled mesh consisting of tetrahedral elements. Mesh sensitivity analyses were performed on the $\varepsilon = 0.8$, 5 mm-length unit cell to optimise element size both for steady-state and transient analyses. The maximum element size was fixed to 0.2 times the cell size (L). Additionally, for the same porosity level, the independence of the numerically calculated λ_{eff} from the length (L) and the number of stacked cells (N) was checked. The values obtained for the 5 mm-length unit cell ($L = 5$ and $N = 1$), considered the reference, and those with $L = 10$ mm and $N = 16$ were evaluated and compared. These values differ by 0.009 % ($L = 5$ mm vs $L = 10$ mm) and 0.5 % ($N = 1$ vs $N = 16$), respectively, confirming that λ_{eff} does not depend on L and N.

As aforementioned, an Al alloy (Al-Si7-Mg0.4, a classical casting alloy also widely available as powder for AM processes) was assigned to the PS and BCC lattices. Paraffins (organic PCM) were assigned to the "void" domains. Regarding the PS, two cases were considered (Fig. 3): case "A", where the same PCM fills both void subdomains and case "B", where the two subdomains are filled by two paraffins (one for each domain) with different melting temperatures (labelled "high-T PCM" and "low-T PCM"). Case A represents a 2-phase C-PCM, while case B is the 3-phase one. In this last case, the two PCM subdomains are equivalent in volume.

To the authors' best knowledge, the current scientific literature is scarce about the thermal characterization of Al-Si7-Mg0.4 produced by AM techniques. For this reason, its thermal properties were selected based on studies on casting products [75–78]. Al-based rapidly solidified products present microstructural changes in the as-produced conditions if thermally treated [79]. These latter variations may modify the properties of the material. Accordingly, the authors selected reasonable simulation values based on the data provided in [75–78]. In any case, the behaviour of the material stabilizes after a certain number of cycles. A preliminary thermal treatment can be considered to stabilize the microstructure [79]. The thermophysical properties of interest were considered temperature-independent since they slightly increase/decrease in the temperature range from room temperature (RT = 298 K) to about 413 K, which corresponds to the maximum temperature value set to this phase during simulations. For the same reason, the properties of the paraffins were considered temperature-independent but different for the solid [80–83] and liquid state [63]. Two paraffins were selected, with melting temperatures of 333 K (*low-T PCM*) and 353 K (*high-T PCM*), respectively. A literature survey was performed for both the PCMs, to retrieve data regarding the thermophysical properties of paraffins with similar melting temperatures. A consistent scattering of these data (solid and liquid phase) was found for the following properties of the *low-T PCM*: C_p (2000–2900 Jkg^{-1} K^{-1} for the solid phase and 2400–2900 Jkg^{-1} K^{-1} for the liquid phase [84–87]); ρ (865–930 kg/m^3 for the solid and 775–830 kg/m^3 for the liquid [83–88]); λ (0.2–0.514 Wm^{-1} K^{-1} for the solid and 0.167–0.4 Wm^{-1} K^{-1} for the liquid [9,58,66,83–93]) and the melting temperature range (6-14 K [9,84,87,93]). Representative values among the proposed ranges were selected to describe the *low-T PCM* (Table 2). The melting temperature of

Table 2
Thermophysical properties of the Al alloy [75], the low-T and high-T PCMs (solid and liquid state) [58,63,80,82,83]. Case A and B refer to the 2- and 3-phase cases (Fig. 3), respectively.

	λ [Wm^{-1} K^{-1}]	ρ [kg/m^3]	Cp [Jkg^{-1} K^{-1}]	α [m^2/s]	T_m [K]	ΔH [J/kg]	ΔT [K]	Case A	Case B
Solid Al alloy	187.5	2588	950	7.6E-05	–	–	–	Yes	Yes
Solid high-T PCM	0.45	920	2300	2.1E-07	353	235,000	10	Yes	Yes
Liquid high-T PCM	0.21	790	2800	9.5E-08					
Solid low-T PCM	0.35	900	2200	1.8E-07	333	235,000	8	–	Yes
Liquid low-T PCM	0.2	785	2600	9.8E-08					

the paraffin was set as the median value of the temperature solidification range. Conversely, to the author's best knowledge, the literature does not offer reliable data for the *high-T PCM*. However, the literature also suggests a slightly increasing trend of the above properties as the number of carbons in the molecular chains increases [63,80–83]. For example, paraffin which melts at 373 K, exhibits $\lambda = 0.665$ Wm^{-1} K^{-1} [93]. Given the collected data, slightly higher values were proposed for the thermophysical properties of the *high-T PCM*. Details are provided in Table 2. On the other hand, the same latent heat of fusion (ΔH) for both PCMs was considered due to its minor dependence on the length of the molecular chains [63]. Although the paraffins considered in this work undergo a solid-solid transition, followed by a solid-liquid one, only one phase change was considered since the transition temperatures are pretty close [82]. Also, in the present case, the latent heat of fusion (ΔH) value was selected based on literature data, where it ranges approximately from 200 to 250 kJ/kg [82,86,91].

Finite Element (FE) analyses were performed to calculate the λ_{eff} in its fully solid conditions. A single-cell structure with adiabatic conditions on lateral surfaces was considered (Fig. 4a). Constant temperatures of 300 and 301 K were set on the top and bottom faces of the unit cell. No heat sources were considered in the material, so the Laplace description [94] of the temperature field was considered [94]. Boundary conditions and reference axes are provided in Fig. 4a. Perfect thermal contact (continuity) was set at the interfaces between different phases. These simulations provided as output the temperature distributions within the cell and the average heat flux normal to the bottom surface (q), which is the one at the lower temperature (z-direction, positive 'entering' the face). From this latter, the effective thermal conductivity was derived as described in Eq. (5) [94]:

$$\lambda_{eff} = -\frac{1}{q}\frac{\partial T}{\partial z} \tag{5}$$

The resulting λ_{eff} of the C-PCMs was then compared to the theoretical limits defined by the phase Wiener bounds (i.e., $\lambda_{\parallel}$ and $\lambda_{\perp}$ in Eqs. (6) and (7), [95]), which define the theoretical maximum/minimum values for λ_{eff}, also dependent on the thermal conductivity of the two phases.

$$\lambda_{\parallel} = (1-\varepsilon)\lambda_{Al} + \varepsilon\lambda_{PCM} \tag{6}$$

$$\lambda_{\perp} = \left(\frac{1-\varepsilon}{\lambda_{Al}} + \frac{\varepsilon}{\lambda_{PCM}}\right)^{-1} \tag{7}$$

In Eqs. (6) and (7), λ_{Al} and λ_{PCM} refer to the thermal conductivity [Wm^{-1} K^{-1}] of the metal and the PCM, respectively (Table 2).

The goodness of the two phases' arrangement in achieving high effective thermal conductivity was estimated through two indexes: 1) the "microstructural efficiency Index" (η), defined in Eq. (8) [95], which allows estimating how close λ_{eff} is to the upper Wiener bound; 2) a "morphological factor Index" (μ, defined in Eq. (9), [95]) which allows understanding how far is λ_{eff} from both limits.

$$\eta = \frac{\lambda_{eff}}{\lambda_{\parallel}} \tag{8}$$

$$\mu = \frac{\lambda_{eff} - \lambda_{\perp}}{\lambda_{\parallel} - \lambda_{\perp}} \tag{9}$$

2.3. Effect of the architecture, porosity and size of the lattice on the thermal response of the C-PCM in transient analyses

Sets of numerical simulations in a time-dependent regime were performed on the C-PCMs proposed with the software Comsol Multiphysics (www.comsol.com) for evaluating their thermal responses under a possible service input. Three different cases were considered. Specifically, Case 1 is conceived to study the impact of the cell type (i.e.,

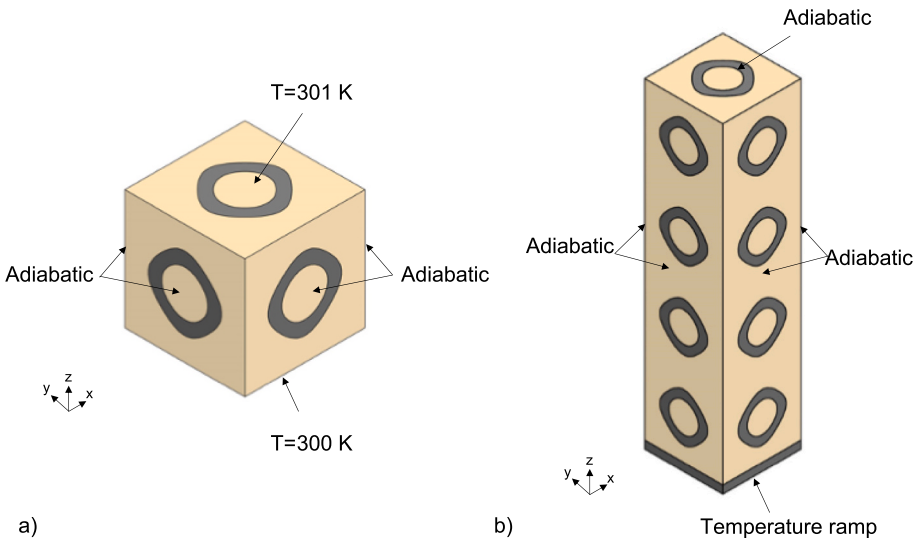

Fig. 4. Reference axes and boundary conditions for the steady-state (a) and transient (b) analyses.

PS vs BCC). Case 2 allows assessing the effect of the porosity (ε) for the PS-based structure. Case 3 is conceived to analyse the influence of the cell size (i.e., L). Case 3 was also selected to display the concurrent effect of boundary conditions. The analyses were performed on the structures listed in the "Transient Analyses" section in Table 1. As clarified in Section 3.1, the choice of these structures has also been motivated by the results obtained from the size-normalised analysis of the unit-cell topologies. We considered the "P-6.67-0.8-3" structure (Table 1) as the reference for all three analysed cases.

For time-dependent analyses, the Laplace equation was modified as described in Eq. (10) [94]:

$$\rho_i C_{p,i} \frac{\partial T_i}{\partial tx} - \lambda_i \nabla^2 T_i = 0 \tag{10}$$

where ρ_i, $C_{p,i}$ and λ_i correspond to the density, specific heat, and thermal conductivity of the i-th phase. For the above cases, in which a 2-phase C-PCM was considered (Case A in Fig. 3), these phases are the Al-Si7-Mg0.4 and the high-melting temperature paraffin. For the 3-phases C-PCM (Case B in Fig. 3) these phases are the Al-Si7-Mg0.4, the high-melting temperature paraffin and the low-melting temperature paraffin. The convective heat transport due to motions within the PCM in the molten state was considered negligible [55].

The same considerations described in the previous section for generating the structures, the type of discretization and the mesh were adopted in the transient analyses. For every C-PCM, an Al-Si7-Mg0.4 plate, having the same cross-sectional area of the composite and thickness of 1 mm, was added at the bottom of the C-PCMs (Fig. 4b). The plate is used to simulate a real application where the heat is supplied homogeneously at one side of a PCM confinement medium, possibly with high conductivity, and it is driven into the composite accordingly to the PCM/Al phase properties and arrangement. Adiabatic boundary conditions were chosen for the C-PCM's top and lateral surfaces. A temperature ramp of 0.0278 K/s (equal to 100 K/h) was applied at the bottom plate of the structure to progressively melt the paraffin (Fig. 4b) for approximately 4050 s. As before, the high-T paraffin was selected for these analyses, and its transition was modelled as a linear function in the 'Phase Change Material' module of the software Comsol Multiphysics (www.comsol.com) on the bases of the material properties reported in Table 2. The RT condition, i.e., 298 K, was selected as the initial condition for the whole C-PCM. After preliminary analyses of time-step sensitivity, the time step for FE simulations was set to 10 s just before the onset of PCM melting (at approximately 1800 s). Then, a refined time step of 0.5 s was chosen to cover the whole transition range. The analyses performed in Case 3 were repeated for the maximum and minimum cell size setting a ramp rate of 0.075 Ks^{-1} (270 K/h) at the bottom surface, initially at RT, to assess the concurrent effect of the boundary conditions. In this case, the time step during melting was reduced to 0.1 s.

The following quantities, most of which are time-dependent and defined considering the end of the i-th time interval, were evaluated for comparing the influence of the design parameters taken into account on the 3 sets of numerical simulations performed (labelled as Case 1, Case 2 and Case 3 in Table 1):

- PCM melting onset time (tx_{on})
- PCM melting offset time (tx_{off})
- PCM melting time interval (Δtx_{melt})
- Volume-averaged liquid fraction ($f_{L,i}$)
- Difference between the volume-averaged temperatures of the metallic and PCM phases ($\Delta T_{Al\text{-}PCM,i}$)
- Rate of change of $\Delta T_{Al\text{-}PCM,i}$ $\left(\left(\frac{\Delta(\Delta T_{Al-PCM})}{\Delta tx}\right)_i = \frac{\Delta T_{Al-PCM,i+1} - \Delta T_{Al-PCM,i}}{tx_{i+1} - tx_i}\right)$
- Liquid fraction rate $\left(LFR_i = \frac{f_{Li+1} - f_{Li}}{tx_{i+1} - tx_i}\right)$
- Power absorbed by the PCM domain ($P_i = DH^{*}LFR_i{}^{*}m$), by definition, proportional to LFR.

A is the area of the plate (Fig. 4b) [m^2], and m is the mass of the PCM [kg].

2.4. Thermal response of the 3-phase C-PCM

A transient study was also performed on the 3-phase C-PCM. As aforementioned, the system is realised with a double organic PCM percolated in the two "void" domains separated by the metallic PS structure (Case B in Fig. 3). The same approach described in Section 2.3 was adopted, considering the addition of the *low-T PCM*. The thermal responses of the 2-phase and 3-phase C-PCMs under the same conditions adopted for the cases 1, 2 and 3 were calculated and compared with the metal structure labelled as P-5-0.8-4 (details in Table 1). The material parameters are provided in Table 2.

Due to the similar thermal conductivities of the selected paraffines, the λ_{eff} of the C-PCMs with 2 or 3 phases was considered to be the same. Indeed, in the solid phase ~~and~~ for $\varepsilon = 0.8$, λ_{eff} differs by 0.09 %. Furthermore, the thermal diffusivity values of the two paraffins (α, calculated on the bases of λ, Cp and ρ listed in Table 2) can be considered the same when both phases are in the solid or liquid state, and when one is liquid and the other is in the solid state. The thermal response of the 2 and 3-phase C-PCMs thus is mainly related to the melting ranges of their PCMs and to the corresponding latent heat fractions stored/released within this range.

3. Results and discussions

3.1. Size-normalised geometrical description of the structures and preliminary C-PCMs feasibility considerations

The correlations between ε and the L-normalised geometrical indexes introduced in Section 2.1 are discussed and summarised in Fig. 5. Fig. 5a compares the d/L trends of the PS and BCC structures. Points were obtained by calculating the d/L ratio for different ε and L values. The selected ε range was 0.68–0.99. 0.68 represents the percolation threshold of the BCC structure as demonstrated in [55], while 0.99 was considered the maximum reachable, theoretically, porosity value. Hence the BCC percolation limit was considered for the PS. For the BCC, a third-order polynomial description proposed by Li and Gariboldi ([55], Eq. (11) in Table 3) and valid in the percolation range up to 0.99 is mapped in Fig. 5a. This trend is almost linear up to $\varepsilon = 0.85$. Above this value, the ε of the BCC structure can be increased by increasing d/L more than linearly. A good agreement was found between the values from Eq. (11) [55] and the computed data (Fig. 5a). For any ε, the L-normalised diameter of the BCC structure is greater than that of the PS. Their relative differences increase with ε (from 12 % to 16 % as ε increases from 0.7 to 0.9). At high ε values, a linear correlation is obtained for d/L (Fig. 5a), t_{min}/L, t_{max}/L (Fig. 5b) and Bd/L (Fig. 5c) for the PS skeleton. Further, as ε increases up to 1, the L-normalised thicknesses values go to zero, while the d and Bd diameters (Fig. 2) are those of the PS minimal surface. Fig. 5a shows that the linear trends for PS structure are valid for ε values down to 0.68, which is the BCC percolation limit. The best-fitting linear correlations in the porosity range of 0.68–0.99 are listed in Table 3 (Eqs. (13), (14), (15) and (17)). The comparison between Eqs. (14) and (15) shows that t_{max}/L is approximately 21 % bigger than t_{min}/L at $\varepsilon = 0.68$. Further, the t_{min}/L trend is similar to the thickness data (Fig. 5b, red line) derived from Bonatti et al. [68].

Fig. 5c shows the Bd/L trend for the BCC structure, based on the analytical description obtained from Eq. (12). Up to about $\varepsilon = 0.87$, the Bd/L ratio of the PS structure is bigger than that of the BCC structure, suggesting in this range a potentially simpler PCM percolation during the PS-based C-PCM fabrication.

The metal skeleton can be created once the cell type, the ε (or v_s) and L values are settled. However, these parameters alone are not enough to thoroughly check the manufacturability of the C-PCMs. As already explained, further geometrical aspects should be included, such as Bd

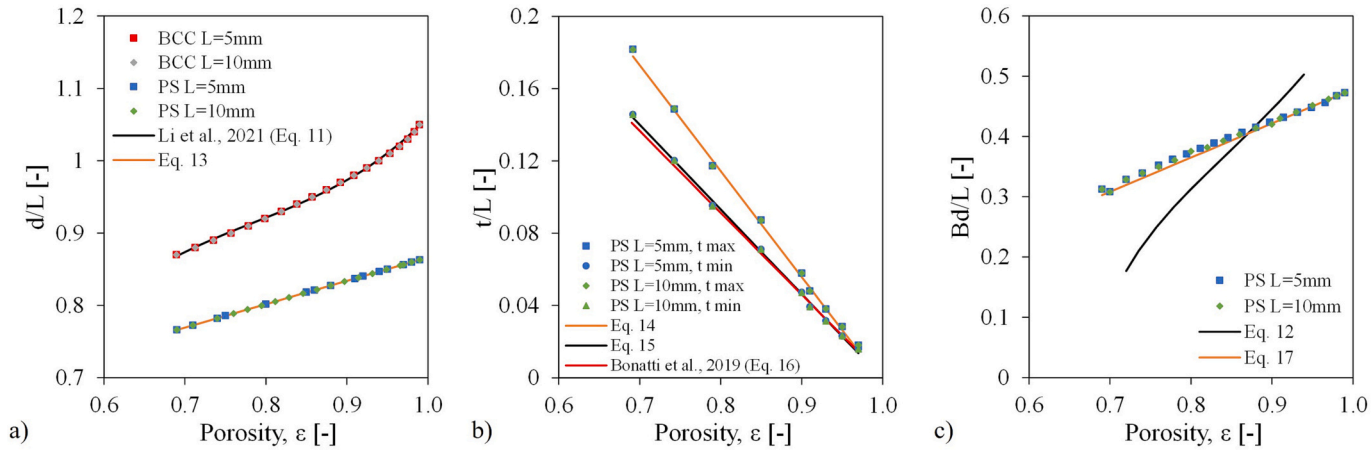

Fig. 5. Correlations between the ε and L-normalised parameters for the PS and BCC lattices obtained at different L values (5 and 10 mm) in the 0.68–0.99 ε range. a) d/L for both PS and BCC lattices. b) t_{min}/L and t_{max}/L for the PS lattice. c) Bd/L for the PS and BCC lattice. Data obtained from the literature are plotted together with the fitting curves provided in Table 3.

Table 3
Analytical equations describing the variations of the design parameters selected for the PS and BCC lattices. Eqs. (11) and (16) were extrapolated from [55,68]. Eqs. (12), (13), (14), (15) and (17) were derived from fitting the measured geometrical data (Fig. 5).

Cell type	Equations		
BCC	$d/L = 4.969\varepsilon^3 - 11.683\varepsilon^2 + 9.599\varepsilon - 1.825$		(11)
	$Bd/L = ((d/L)^2 - 0.75)^{0.5}$	With $0.72 < \varepsilon < 0.94$	(12)
PS	$d/L = 0.3227\varepsilon + 0.5435$	With $0.68 < \varepsilon < 0.99$	(13)
	$t_{max}/L = 0.5623*(1-\varepsilon)$	With $0.68 < \varepsilon < 0.99$	(14)
	$t_{min}/L = 0.4615*(1-\varepsilon)$	With $0.68 < \varepsilon < 0.99$	(15)
	$t/L = 0.4529*(1-\varepsilon)$		(16)
	$Bd/L = 0.5671\varepsilon - 0.0887$	With $0.68 < \varepsilon < 0.99$	(17)

and d as a function of L. Specifically, the L value can be limited upward by d to print a self-supporting structure. The L bottom limit is instead linked to the minimum printable thickness (t_{min}) and the minimum diameters of the open-cell structure (Bd), which allow the structure to be filled by the molten PCM and to be cleaned from the unmelted powder, after the printing process. The equations provided in Table 3 are thus conceived to support the dimensioning of the C-PCMs. Once assigned the ε and L values, the others can be immediately derived and thus verified to check whether they fall within suitable ranges according to the selected material, printing technology, and paraffin. PS structures can be manufactured, as demonstrated in [18] for Ti-6Al-4 V and Hastelloy-X via laser powder bed fusion (L-PBF), with L in the 3.3–10 mm range and a thickness in the 0.265–2.07 mm range. For example, bigger lattices (L = 12.7 mm, thickness in the 0.37–1.11 mm range) were printed in PA12 with the Selective Laser Sintering technology [96]. For Al-alloy lattices, a PS structure with L = 10 mm was recently produced by L-PBF in AlSi10Mg with ε = 0.8, corresponding to d = 8 mm [97]. Based on the authors' experience, an Al-Si7-Mg0.4. BCC lattice with ε = 0.8 and L = 5.5 mm (corresponding to d = 5.07 mm) is manufacturable. Independently on these, the correlation in Fig. 5a suggests that, for the same porosity values, and cell size (L), a PS structure has a smaller d value than the BCC. Hence, the risk of collapse during printing could be reduced. Thus, upper L = 10 mm and L = 9 mm limits can be considered for the Al PS and BCC structures, respectively (with ε = 0.8) [97]. However, these limits are mainly indicative since they depend on the selected material, printing technology and machine.

From the point of view of AM feasibility, the PS structure is characterised by a continuous thin structure that requires good tolerance to ensure the desired thermal resistivity. Poltue et al. [69] report a series of Sheet TPMS structures (Primitive-Schwarz, Gyroid, Diamond, Neovius, Schoen F-RD and I-WP) manufactured via L-PBF with Ti-6Al-4 V alloy, with thicknesses in the 0.1–0.3 mm range and d in the 0.3–0.6 mm range. With the same technology, PS structures made of 304 stainless steel were manufactured with a t ranging from 0.4 to 0.6 mm [98]. More recently, a PS structure was produced in AlSi10Mg by L-PBF with t = 0.1 mm and L = 5 mm [99]. It is thus possible to assume that 0.1 mm, despite being a challenging value, could represent a lower limit for manufacturing metal Sheet-based PS lattices. Conversely, no data for the Bd value (Fig. 2) are available. However, the authors filled Al alloy lattice structures with Bd = 1.6 mm without problems. 1.2 mm can be considered as the Bd minimum value, considering the necessity to fill in the structure at a relatively high temperature since the viscosity of paraffins decreases significantly as the temperature exceeds the melting completion [63]. Hence, based on these considerations, the C-PCM structures, considered for the transient analyses (as described in Section 3.3 and shown in Table 1) were dimensioned inside these reference limits. This "geometrical" analysis has been thus fundamental to drive the rest of the study.

The surface-to-volume ratios can be considered design parameters for C-PCM structures, even if they do not strictly affect the processability of the metallic skeleton or its filling with the PCM in the molten state. For this reason, they will be considered for evaluating the thermal behaviour of the C-PCMs. However, in this case, differences exist between the classical literature approach considering only the metallic skeleton structures surrounded by non-thermally conductive, non-dense fluid and C-PCMs where a low-conductivity PCM fills the empty space. In the former case, the surface/volume interface of the solid is considered, and instead, in the latter, the surface-to-volume interface of the PCM also has to be considered. As for the analytical description introduced in Section 2.1 (Eqs. (3) and (4)), the R_{Al} and R_{PCM} parameters are presented in Fig. 6, together with their best-fit curves provided in Table 4. Fig. 6a, Eq. (18) (for the BCC) and Eq. (20) (for the PS) show that the R_{Al} values of both structures increase as ε approaches 1. This increase is particularly steep for the PS structure, in agreement with Abueidda et al. [70]. At ε = 0.97, the R_{Al} of the PS structure is about twice that of the BCC. Conversely, R_{PCM} presents a monotonically decreasing trend as ε increases. This trend is steeper for the BCC structure (Fig. 6b, Eqs. (19) and (21) for the BCC and PS structures, respectively). This situation is particularly favourable for the PS structures at a high ε. Indeed, at ε = 0.97, the R_{PCM} of the PS is twice that of the BCC. This result means that the PS topology favours the heat flow from the PCM phase to the metal structure and vice versa. Size-dependent expressions of the surface-to-volume ratios can be easily obtained by dividing R_{Al} and R_{PCM} by L.

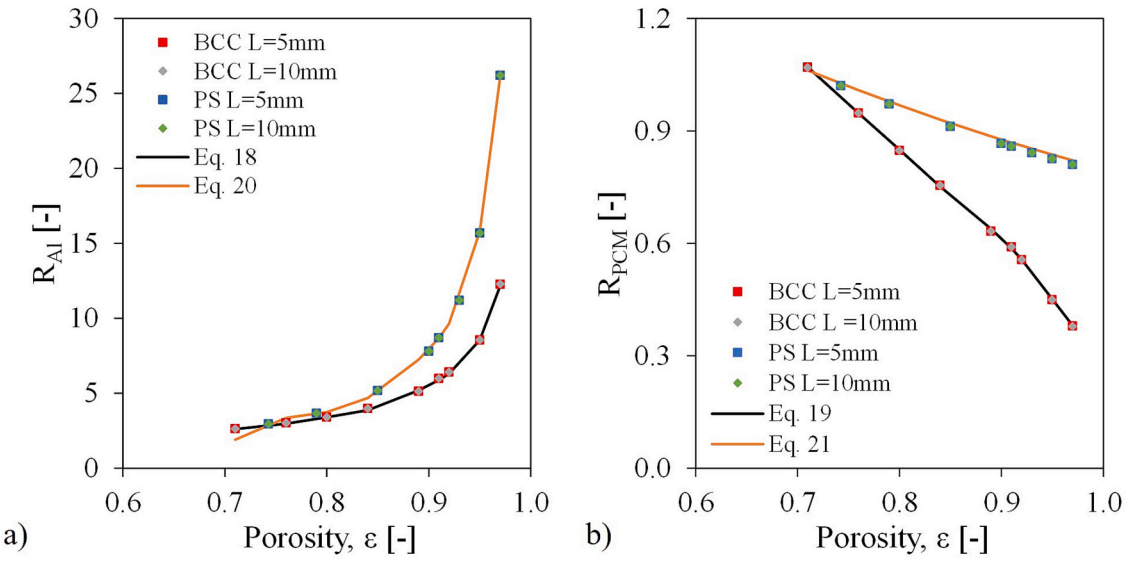

Fig. 6. Length size-normalised indexes R_{Al} (a) and R_{PCM} (b) for the BCC and PS structures (Eqs. (3) and (4)). Values obtained with ε ranging from 0.72 to 0.97.

Table 4
Equations for the normalised surface-to-volume ratios, R_{Al} and R_{PCM}, of both C-PCMs (Eqs. (3) and (4)), derived by best fitting data presented in Fig. 6.

Cell type	Equations		
BCC	$R_{Al} = 1{,}218{,}029.8\varepsilon^6 - 6{,}072{,}075.9\varepsilon^5 + 22372432\varepsilon^4 - 24301569\varepsilon^3 + 14{,}817{,}979.9\varepsilon^2 - 4{,}808{,}727.1\varepsilon + 648{,}825.9$	With $0.72 < \varepsilon < 0.97$	(18)
	$R_{PCM} = 24{,}924.2\varepsilon^6 - 125660\varepsilon^5 + 263.241.8\varepsilon^4 - 293306\varepsilon^3 + 183{,}332.4\varepsilon^2 - 60{,}956.7\varepsilon + 8424.9$	With $0.72 < \varepsilon < 0.97$	(19)
PS	$R_{Al} = 2{,}234{,}097.7\varepsilon^6 - 10{,}962{,}975.3\varepsilon^5 + 22372432\varepsilon^4 - 24301569\varepsilon^3 + 14{,}817{,}979.9\varepsilon^2 - 4{,}808{,}727.1\varepsilon + 648{,}825.9$	With $0.72 < \varepsilon < 0.97$	(20)
	$R_{PCM} = 0.7\varepsilon^2 - 2.1\varepsilon + 2.2$	With $0.72 < \varepsilon < 0.97$	(21)

3.2. Effective thermal conductivity for steady-state analyses

In addition to the thermal conductivities of the single phases, the λ_{eff} of the C-PCM depends on ε and its arrangement inside the lattice bounding box. The correlation among the thermal conductivity of the BCC and PS C-PCM structures and ε can be found in Fig. 7a, together with the upper and lower bounds (Eqs. (6)–(7)), drawn as black and green dashed lines, respectively. These bounds, both decreasing when ε increases, significantly differ due to the almost 3 orders of magnitude in the Al alloy and PCM thermal conductivity. Within these limits, in the 0.68–0.99 porosity range, the thermal conductivity of BCC and PS structures have similar values, not far from the upper bound ($\lambda_{\parallel}$, "Parallel" in Fig. 7a).

However, λ_{eff} of PS structures is closer to the upper limit than BCC, exhibiting an advantageous arrangement in the studied range (Fig. 7a). This evidence is well described by the trends of the η and μ indexes (Eqs. (8)–(9), Fig. 7b and c). In the 0.68–0.99 ε range η and μ of the BCC drop progressively to 0.25 and 0.17 of $\lambda_{\parallel}$, respectively. On the contrary, in the PS structure, both indexes are higher and remain close to 0.7, with an average η value of 0.676 in the 0.8–0.98 ε range. This means that in this porosity range, λ_{eff} is 67.6 % of the theoretical maximum. Thus, λ_{eff} can be easily estimated from Eq. (22) without requiring numerical simulations for the specific unit cell. This porosity range (0.8–0.98) is thus interesting for creating PS-based C-PCM composites with a high conductivity matrix.

$$\lambda_{eff} = 0.676[(1-\varepsilon)\lambda_{Al} + \varepsilon\lambda_{PCM}] \quad (22)$$

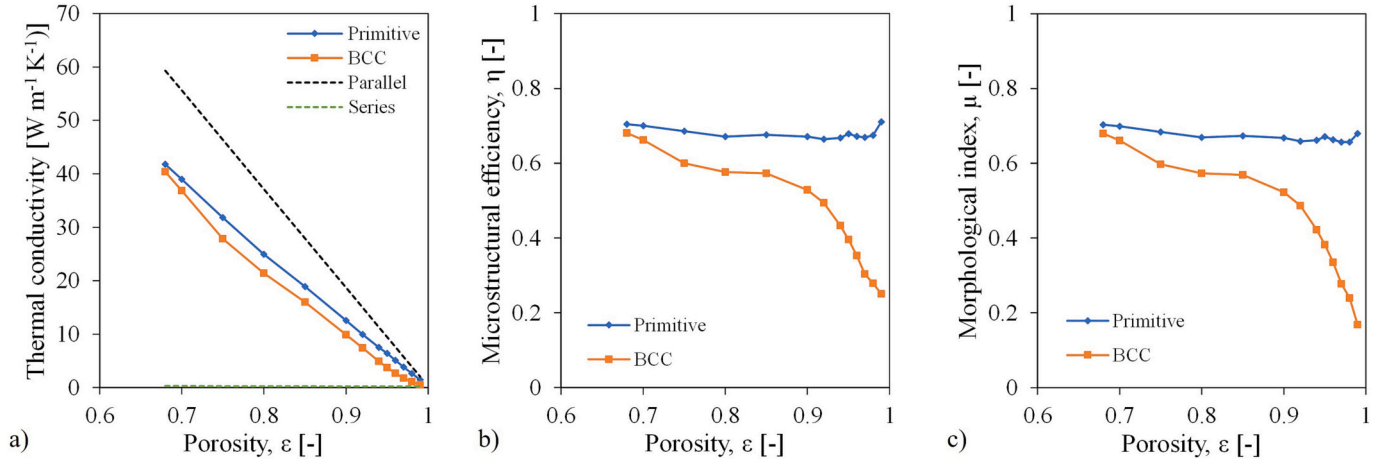

Fig. 7. a) Effective thermal conductivity (λ_{eff}) of the BCC and PS structures as a function of the porosity. The Wiener bounds ($\lambda_{\parallel}$ and $\lambda_{\perp}$, "Parallel" and "Series", respectively) are also mapped. b) and c) show the microstructural efficiency index η) and the morphological efficiency index (μ) as a function of the porosity (ε), respectively.

It is worth mentioning that the trends of the efficiency indexes are strongly correlated to the thermal conductivity of the phases of the composite and their relative ratio ($\lambda_{Al}/\lambda_{PCM}$) [95]. Hence, these considerations and Eq. (22) are valid for a ratio of skeleton-to-filler-thermal-conductivities of about 400 (417 is the value obtained as 187.5/0.45, Table 2). It is also worth mentioning that most of the C-PCM structures used in Cases 1, 2, and 3 and for the 3-phase C-PCM have the same porosity ($\varepsilon = 0.8$) but different lattice lengths. However, their λ_{eff} is the same (about 25 Wm^{-1} K^{-1}). Instead, the λ_{eff} of the metal PS-based C-PCMs is 14 % higher than that of the BCC. As shown in the next sections, λ_{eff} is one of the parameters which regulates the readiness of the C-PCM thermal response.

3.3. Effects of cell architecture, porosity and size in transient analyses of 2-phase C-PCMs

As discussed in Section 2.3, 3 sets of numerical simulations in the transient state were performed on 2-phase C-PCMs (Table 1) to evaluate the influence of the design choices on their thermal responses. These C-PCMs fall within (and often close) the upper and lower manufacturability bounds defined in Section 3.1 for the PS structures. The results of the 3 sets of transient analyses are compared considering, in addition to the times for the PCM melting onset and completion (these are standard parameters to compare the thermal behaviour of C-PCM), also the punctual and the average thermal response of the C-PCM structures. Table 5 (as shown in Section 2.2) provides the PCM melting onset/offset times. The PCM melting starts simultaneously ($tx_{on} = 1810$ s). Indeed, the PCM at the bottom of the lattice reaches the temperature for its melting onset, independently of the phase arrangement, the lattice size and the porosity ratio. The time interval for PCM melting (Δtx_{melt}) and the PCM melting offset time (tx_{off}) are adopted in the scientific literature on C-PCMs to evaluate the performance of heat storage or heat management systems [58]. The former (Δtx_{melt}) can be exploited to design structures optimised for cyclic service, where the time for forward/backward PCM transformation (i.e., heat storage+release time) should correspond to the cycle time. On the other hand, when the C-PCM structure needs to accumulate heat starting from RT or is designed to prevent overheating, tx_{off} becomes the reference parameter. Notwithstanding the same λ_{eff}, Δtx_{melt} and tx_{off} vary for the 2-phase PS structures characterised by different L values at $\varepsilon = 0.8$, as shown in Table 5 (and described in Section 3.2).

To analyse the local thermal response differences, the temperature and liquid volume fraction in the PCM phase were compared at the standard heating rate (0.0278 K/s) and at a fixed time (i.e., 2100 s, Table 6). This time guarantees a sufficiently high average volume fraction of molten PCM. The time-evolution of the volume-averaged parameters considered in this paper ($\Delta T_{Al\text{-}PCM}$, f_L, *LFR* and *P*) are presented for the same C-PCM structures in Figs. 8a-c, respectively. The effect of each parameter is analysed separately in the corresponding case (Case 1, 2, and 3).Case 4 refers to the comparison between 2- and 3-phases C-PCMs.

Table 5
PCM melting onset/offset times (tx_{on} and tx_{off}, respectively) and melting time intervals (Δtx_{melt}) for the C-PCMs. P-6.67-0.8-3 represent the reference structure used for various comparisons.

Structure	Case	tx_{on} [s]	tx_{off} [s]	Δtx_{melt} [s]
B-6.67-0.8-3	1	1810	2386	576
P-6.67-0.8-3	1, 2, 3	1810	2352	542
P-6.67-0.9-3	2	1810	2504	694
P-5-0.8-4	3, 4	1810	2338	528
P-4-0.8-5	3	1810	2323	513
P-3.33-0.8-6	3	1810	2317	507
P-6.67-0.8-3-270 K/h	3	677	965	288
P-3.33-0.8-6-270 K/h	3	677	932	255
3p-P-5-0.8-4	4	1129	2305	1176

3.3.1. Case 1: effect of the metallic phase cell type

Case 1 compares the C-PCMs B-6.67-0.8-3 and P-6.67-0.8-3, which only differ for the cell type (Table 1). Their porosity ($\varepsilon = 0.8$) is relatively high, ensuring percolation and good thermal storage potential. Their cell size is $L = 6.67$ mm, the maximum considered in the present work, which assures printability and reasonably the absence of convection motions in both structures. The local temperature and PCM liquid fraction distributions, shown for these structures at $tx = 2100$ s in the first row of Table 6, highlight the highly inhomogeneous global temperature distribution for both structures. The punctual behaviour is quantified utilizing two points laying on the same mid-height plane of the unit cell: point "A" is at the centre of the PCM sphere inscribed in the structure (Fig. 2a and b), while point "B" is at the interface between the PCM and the metal domain. In the BCC structure, the distance between the two points is $d/2$. In the PS structure, this distance is slightly bigger than $d/2$ (Fig. 2). The onset and completion of melting at point A are shorter in the PS-based C-PCM (Table 7). The maximum temperature difference between B and A ($\Delta T_{B\text{-}A}$) is higher for the BCC structure (Table 7). This result confirms the presence of more pronounced temperature inhomogeneities within the BCC-based C-PCMs. Generally, the maximum temperature difference between the two phases is achieved during the paraffin solid-liquid transition for all the studied structures, as demonstrated by the classical time-temperature profiles in Fig. 8. Indeed, the phase change triggers the heat absorption at quasi-constant temperature as latent heat of transformation, reducing the temperature increase in the cell for both the PCM and Al, with a more intense effect on the former. However, the average temperature gradient between B and A ($\Delta T_{B\text{-}A}/dx$) is lower for the BCC structure (Table 7) due to the bigger d value at the denominator. Hence, further analyses were necessary to clarify these aspects.

The behaviour deduced by punctual analysis in Table 7 has been then compared to the volume-averaged indexes given in Fig. 9 for the B-6.67-0.8-3 (dotted black lines) and the P-6.67-0.8-3 (solid black lines) structures. Fig. 9a shows that the profiles of the difference between the volume averaged temperatures of the metallic and PCM phase ($\Delta T_{Al\text{-}PCM}$) are characterised by a peak starting at tx_{on} (about 1810 s) and prolonging after tx_{off}. It can be also observed that 2100 s, i.e., the time selected to display the behaviour for different C-PCMs in Cases 1, 2 and 3 is in the increasing part of the $\Delta T_{Al\text{-}PCM}$ time profiles, not far from the peak times. The PS-based C-PCMs have a lower and narrower peak than the BCC.

The comparison between the two arrangements of the metal skeleton phase can also be performed on the more conventional average liquid fraction curve (f_L, Fig. 9b). This curve shows a gradual increase of the liquid phase in all the structures under the simulated service conditions. The development of the volume fraction of liquid in BCC-based C-PCM is slower than that in the PS-based one. The liquid fraction rate (*LFR*, Fig. 9c) represents the first derivative of the f_L-tx curve and is proportional to the latent heat power *P* 'stored' in the PCM phase. Their profiles, given on two scales in Fig. 9c, are characterised by a broad peak that develops on the transition time interval Δtx_{melt}. The power transferred to the PCM is higher in the PS structure, corresponding to a higher latent heat storage power. Indeed, the more massive PCM regions localized in the BCC tend to slow heat diffusion during their melting.

The combination of local and averaged data suggests that, during the peak (Fig. 9a) roughly corresponding to the phase transformation of the PCM, the PS structure has a more homogeneous temperature distribution along the z direction, reached through a more effective local heat transfer at the interface between the high and the low thermally conductive phases.

The advantageous morphology of the PS architecture when faster transients are requested is thus clear. This behaviour can be justified by the higher λ_{eff} and R_{PCM} (Fig. 6b) values for the PS-based C-PCM at the ε considered. Further, the presence in its metallic skeleton of lower d values (Figs. 2 and 5a) than the BCC metal structure can also play an important role, as it will be pointed out later when discussing Case 3.

Table 6
Temperature profiles on the axial mid-section and liquid fraction evolution of the C-PCMs, all at 2100 s, when the "high-T" paraffin of the analysed C-PCMs undergoes the solid-liquid transition.

Case 1 – cell type effect		*Case 2 – porosity effect*			
Inverse BCC		Sheet-based Primitive			
B-6.67-0.8-3		P-6.67-0.8-3		P-6.67-0.9-3	
Temperature [K]	Liquid fraction [-]	Temperature [K]	Liquid fraction [-]	Temperature [K]	Liquid fraction [-]
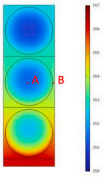	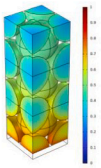	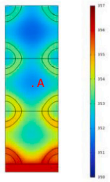	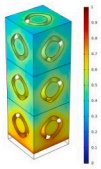	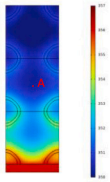	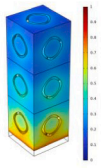

Case 3 - cell size effect					
Sheet-based Primitive					
P-5-0.8-4		P-4-0.8-5		P-3.33-0.8-6	
Temperature [K]	Liquid fraction [-]	Temperature [K]	Liquid fraction [-]	Temperature [K]	Liquid fraction [-]
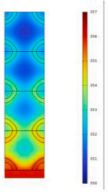	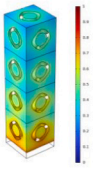	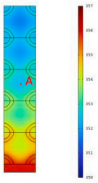	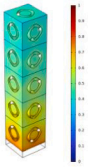	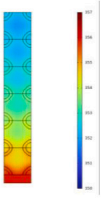	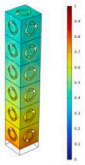

2 and 3-phase composites – Case 4 (Sections 2.4, 3.4)			
Sheet-based Primitive			
P-5-0.8-4		3p-P-5-0.8-4	
Temperature [K]	Liquid fraction [-]	Temperature [K]	Liquid fraction [-]
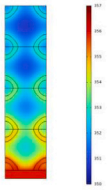	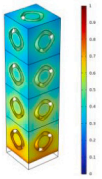	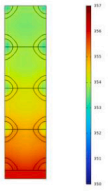	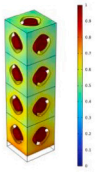

3.3.2. *Case 2: effect of the porosity on the PS structure*

The P-6.67-0.8-3C-PCM (reference structure, as shown in Table 1), introduced in Case 1, is now compared to another C-PCM, i.e., P-6.67-0.9-3, characterised by the same PS metal lattice and lattice size, but a higher porosity ($\varepsilon = 0.9$). The P-6.67-0.9-3C-PCM has about 50 % lower λ_{eff} and lower heat exchange surface for the PCM (R_{PCM}), smaller t_{min} ($t_{min} = 0.301$ mm) and higher "d" than the P-6.67-0.8-3.

The results of the simulated transient behaviour for the P-6.67-0.9-3C-PCM, as expected, are: 28 % longer time intervals for having its solid-liquid transition completed (Table 5, Fig. 9b) and a correspondingly smaller average *LFR* (Fig. 9c). Even if the phase transition and the corresponding power (stored as latent heat) of the P-6.67-0.9-3C-PCM spread over a wider period, their trends are similar to the case of the reference structure (i.e., P-6.67-0.8-3). Further, the lower effective thermal conductivity of the P-6.67-0.9-3C-PCMs leads to the higher average temperature difference within the system before the PCM melting, roughly corresponding to the horizontal trends in the $\Delta T_{Al\text{-}PCM}$ profile (as shown in Fig. 9a for $tx < 1810$ s). The visual comparison of temperature and liquid phase distributions in the first row of Table 6 and the data in Table 7 (greater Local Maximum $\Delta T_{B\text{-}A}$ and $\Delta T_{B\text{-}A}/dx$) suggest that the temperature distribution within the PCM phase is less homogeneous for P-6.67-0.9-3C-PCM, i.e., at higher porosity.

The differences in the behaviour of the two structures can be explained as follows. The structure with the higher porosity (i.e., 0.9 vs 0.8), has a higher amount of low-thermal diffusivity PCM phase, and thus a metal phase with a smaller t_{min}, leading to higher thermal resistance. On the other hand, as the porosity decreases, the latent heat storage reduces since the amount of paraffin per unit volume lowers and, even more, the storable latent heat per unit mass.

Therefore, the beneficial effect of high-porosity lattice structures in terms of thermal storage potential (and an overall effective density reduction for the C-PCMs) has to be carefully considered since it increases the PCM melting time and spreads the power of latent heat storage over a wider time span. Case 2 demonstrates the importance of λ_{eff} in tuning the response of organic-metallic C-PCMs and the importance attributed to its calculation for C-PCM systems [8,52].

3.3.3. *Case 3: effect of the cell size on the PS structure*

Case 3 compares the transient behaviour of four PS structures with the same ε and various L, considering the standard or a high heating rate at the bottom (100 and 270 K/h, respectively; as shown also in Fig. 4). Due to the geometrical parameter selection, the selected four C-PCMs (Table 1) have equal λ_{eff}: their behaviour under steady conditions is the same. The melting times are provided in Table 5. The temperature and

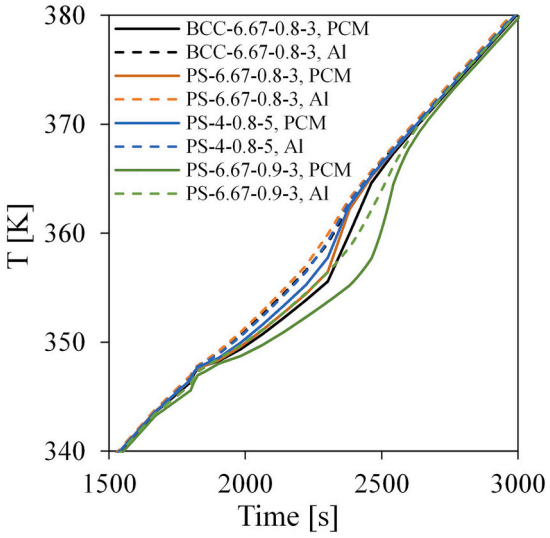

Fig. 8. Time-temperature profiles related to points A in the PCM phase and B in the Al domain for various structures.

Table 7
Melting times at the centre of the PCM sphere in mid-height cell (A, Fig. 2), maximum temperature difference ($\Delta T_{B\text{-}A}$) between PCM/Al interface at the same height (B and A), and the corresponding average temperature gradient ($\Delta T_{B\text{-}A}$/dx) between the points A and B (as shown in Fig. 2).

Structure	Case	tx_{on} at point A [s]	tx_{off} at point A [s]	Δtx_{melt} at point A [s]	Local maximum $\Delta T_{B\text{-}A}$ [K]	$\Delta T_{B\text{-}A}$/dx [K/mm]
B-6.67-0.8-3	(Case 1)	1870	2347	477	3.48	0.55
P-6.67-0.8-3	(Case 1, 2, 3)	1867	2324	457	3.44	0.64
P-6.67-0.9-3	(Case 2)	1900	2468	568	4.47	0.8
P-4-0.8-5	(Case 3)	1853	2307	454	1.5	0.47
P-6.67-0.8-3-270 K/h	(Case 3)	735	928	193	6.8	1.27

PCM liquid fraction distributions at 2100 s obtained with standard heating rate are summarised in Table 6, first and second rows. The corresponding time-evolution of the volume-averaged parameters is shown in Fig. 9, where the trends for the P-5-0.8-4, P-4-0.8-5 and P-3.33-0.8-6C-PCMs are drawn as blue, orange and green solid lines, respectively.

Table 5 shows that the C-PCM with the smallest cell size ensures the fastest response under both heating rates. Fig. 9b shows that the C-PCM with $L = 3.33$ mm has the quickest solid-liquid transition. Similarly to what was observed in cases 1 and 2, Fig. 9c shows that during the phase transition, the LFR and P slightly increase as the cell size decreases from 6.67 to 3.33 mm, displaying in all cases a similar trend. The visual comparison of the images of these structures at 2100 s in the second row of Table 6 shows a tendency towards more homogeneous temperature distributions in the smaller structure ($L = 3.33$ mm). The homogeneity is confirmed by the lowering and narrowing of the $\Delta T_{Al\text{-}PCM}$ peaks as the cell size decreases (Fig. 9a). This can be attributed to a homogeneous capillary distribution of the high-thermally conductive Al alloy phase in the whole structure. Al-Si7-Mg0.4 arrangement in smaller cell size C-PCM, responsible for smaller d values and, in general, less extended PCM domains, allows a more efficient heat transfer from this latter to all the low thermally conductive regions. Smaller cells favour heat transfer towards the PCM volume since the absolute surface-to-volume ratio values for both Al and PCMs increase (obtained by dividing by L the corresponding L-normalised indexes). Smaller cells also shorten the maximum distance between PCM point A and the Al/PCM interface, identified by the B point (Fig. 2).

The influence of d (Fig. 2) on the PCM melting time interval referred to the whole structure is visually presented in Fig. 10. The results for the PS structure are plotted for 2 different heating rates at the bottom surface. The trends suggest that a decrease of d at least in the investigated cell size range, slightly improves the thermal response and heat storage readiness. Fig. 10 also shows that the absolute value of melting time (Δtx_{melt}, Table 5) increases roughly by the same amount – approximately 30 s - moving from 6.67 mm to 3.33 mm cell sizes under the two investigated heating rates (i.e., 100 K/h and 270 K/h). However, the decrease in melting time occurring for the finest structure should be compared to Δtx_{melt}, mentioned in Section 3.3, which is used to adjust the PCM response to the requirements of a LHTES system. Indeed, L-dependence becomes increasingly relevant as the heating rate increases, as suggested by an almost 13 % increase of the Δtx_{melt} of the biggest structure compared to the smallest one. This means that, under this condition, the change in Δtx_{melt} should be considered in the design phase of C-PCMs-based TES systems working under cyclic conditions. Moreover, as the heating rate increases (Table 7), the temperature difference

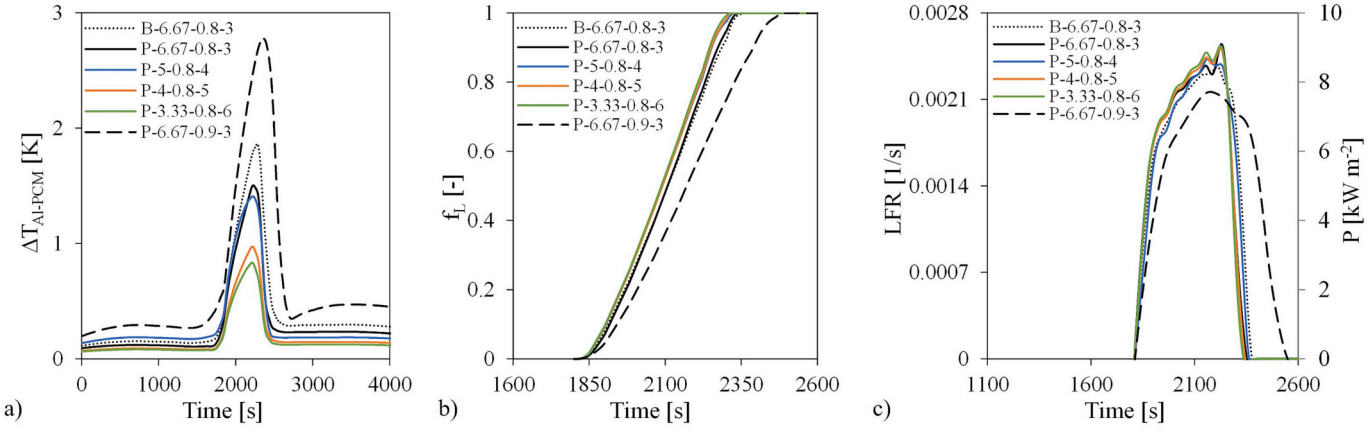

Fig. 9. Cases 1, 2 and 3: effect of the design parameters (Section 2.3) on the thermal response of the C-PCMs architectures. a) Difference between the volume averaged temperatures of the metallic and PCM phase. b) Volumetric average of liquid fraction. c) Rate of liquid fraction change (LFR) and latent heat storage power (P).

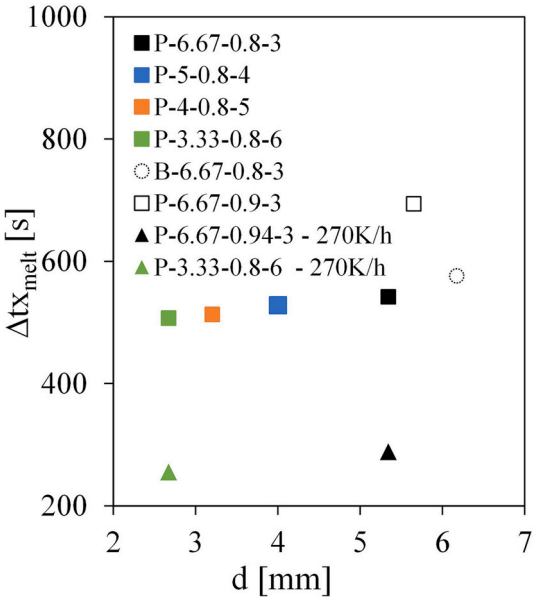

Fig. 10. Case 2: PCM melting time interval (Δtx_{melt}) vs maximum sphere diameter (d) trend for different L values for the BCC and PS-based C-PCMs here investigated. For 2 PS structures of the same geometry, a heating rate of 270 K/h (triangles) was added to the standard one (100 K/h, squares and circles).

between points A and B increases (Table 7).

The critical role played by the metal cell size (L) reduction in shortening melting and improving at the same time the power stored/released as PCM latent heat is evident in Case 3. Fig. 10 also displays the point corresponding to the BCC structure considered in Case 1 (empty dotted circle, B-6.67-0.8-3), which is not far from the Δtx_{melt} vs d trend of the PS structures. The slower heat storage of BCC-based C-PCM can thus be attributed not only to its lower λ_{eff}, but also to its bigger d than the PS.

The analysis of Case 3 results highlights that the design of C-PCMs based on lattice structures filled with organic PCMs cannot be based only on the effective thermal conductivity of the structure. Critical design parameters are also the lattice cell size (L) [55] and the maximum diameter d of the sphere (Fig. 2), for which a correlation exists for any specific lattice structure (for other TPMS topologies at low-medium ε refer to [67]). L and d indeed influence the duration of the transients, together with the structure manufacturability.

3.4. Case 4: transient analyses of 3-phase C-PCMs

This section compares the thermal behaviour of a 2-phase C-PCM and that of a 3-phase one. Metal PS skeletons with $L = 5$ mm and $\varepsilon = 0.8$ were considered, with both void subdomains filled by high-melting paraffin (P-5-0.8-4) or with one of them filled by low-melting paraffin and the other by the high melting one (3p-P-5-0.8-4). Results were obtained under the standard heating rate conditions adopted for Cases 1, 2, and 3 and are summarised in Table 5 and Fig. 11 (P-5-0.8-4 profiles are plotted as blue lines while the 3p-P-5-0.8-4 as red lines). In the examined case, with the selected paraffins having different solid-liquid transition temperatures and with the same specific heating rate and boundary conditions, the time ranges for the phase transitions of the two paraffines do not overlap: one approximately in the 1129–1533 s range and the other approximately in the range 1814–2305 s (Fig. 11a). The horizontal trend at $f_L = 0.5$ of the red line in Fig. 11a further highlights the volumetric equivalence of the PCM subdomains. This simplifies the analysis of the results. Fig. 11a trends are coherent with what is shown in Table 6, last row, where temperature and liquid fraction distributions at 2100 s are presented. In the 2-phase C-PCM, the two PCM domains behave similarly at the same distance from the bottom surface. At the same time, the low-melting paraffin in 3-phase C-PCM is entirely molten. The subdomains containing the low-melting paraffin are consistently warmer and more homogeneous in terms of temperature distributions than the subdomain filled with the high-melting temperature paraffin, which at 2100 s is undergoing a phase transition. This temperature difference between the 2 PCMs phases separated by the Al-alloy sheet at a given distance from the basis of the 3p-P-5-0.8-4 structure influences the thermal interaction between the two PCMs. The difference between the volume-averaged temperatures of the metallic and PCM phases and their time derivatives ($\Delta(\Delta T_{Al\text{-}PCM})/\Delta tx$) have been calculated for both C-PCMs and are presented in Fig. 11b. Focusing the attention on the 2-phase C-PCM, the $\Delta(\Delta T_{Al\text{-}PCM})/\Delta tx$ profile is relatively flat until it soars at the beginning of the PCM melting (as the PCM temperature becomes lower than the Al temperature). For the 3-phase C-PCM, a sequence of two valley-peak can be observed in the $\Delta(\Delta T_{Al\text{-}PCM})/\Delta tx$ profiles of both the low-melting and the high-melting paraffins, confirming the thermal interaction between the two. This means that the phase transition of the low-T PCM causes a heat transfer from the high-melting PCM, with a consequent $\Delta(\Delta T_{Al\text{-}PCM})/\Delta tx$ increase due to the heat absorption offered by the progressive phase change. The inverse situation occurs as the high-melting PCM melts. Thus, thermal buffering between the two PCM phases can be considered. Compared to the 2-phase C-PCM, the strictly interconnected volumes of the 3-phase C-PCM modify heat transfer dynamics with the external environment.

3-Phase C-PCM displays a short time for the start of the heat storage, corresponding to the onset of the melting of the Low-T PCM. Moreover, a longer Δtx_{melt} to the completion of the latent heat storage absorption is needed (Table 5) because the completion of melting coincides with the offset of the melting of the *high-T PCM*. This offset is not far from that for

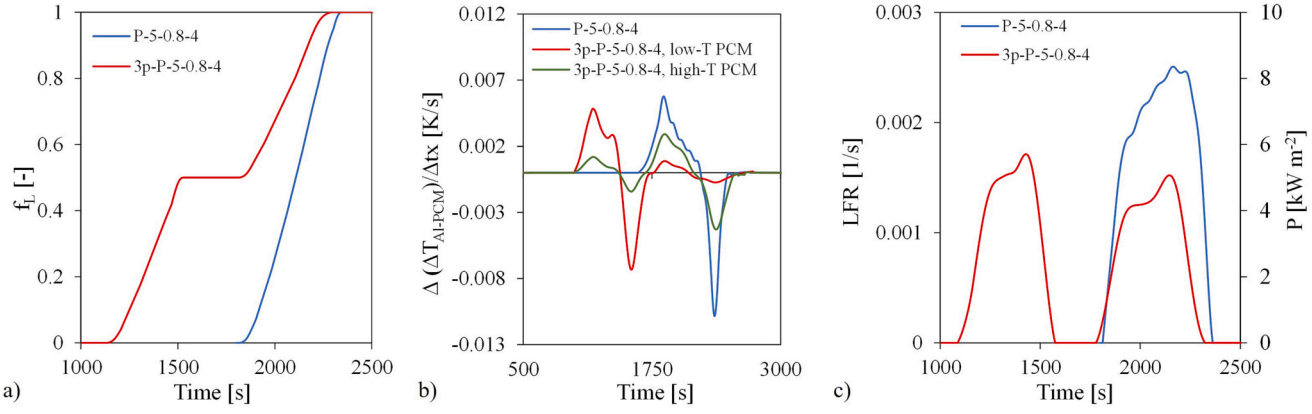

Fig. 11. Effect of the number of phases on the thermal response of the C-PCMs architectures. a) Volumetric average of liquid fraction. b) Time-derivative of the difference between the volume averaged temperatures of the metallic and PCM phases. c) Rate of liquid fraction change, LFR, and power absorbed (P).

the melting of the same paraffin in the 2-phase PCM (Table 5). The small-time differences in the offset time are at least partly due to the minimal changes in the thermophysical properties of the two paraffines. Their melting at different time ranges leads to the two *LFR* (and *P*) peaks (Fig. 11c). The 3-phase C-PCM displays lower average liquid fraction rates (i.e., *LFR* in Fig. 11c) and lower power absorption (i.e., *P* in Fig. 11c) than the 2-phase C-PCM, with one paraffin (i.e., P-5-0.8-4 in Fig. 11c).

Wide melting ranges and low heat storage power are not generally desired in thermal energy storage systems unless the temperature at which the heat is supplied, or the dynamics of the temperature change or of the heat supply to the C-PCM structure is not regular or not well known.

These results also highlight the possibility of coupling the 3-phase PS-based C-PCMs with other devices whose efficiencies are temperature dependent, guiding them towards the desired temperature range defined by the melting temperatures of the two PCMs to maximise their performances. Batteries [100], solar panels [101] and thermoelectric modules [102], for instance, can take advantage of this technology. Such behaviour is absent in the case of the 2-phase C-PCM. Besides, several other thermal storage or management options can be explored by considering the filling of the 2 subdomains by different PCMs, with different non-interconnecting subdomains, as in the Sheet-based PS. Their exploration is far beyond the aim of the present work.

4. Conclusions

In this study, the potentiality of combining organic Phase Change Materials with metallic Sheet-based Primitive-Schwarz (PS) TPMS lattice for obtaining a C-PCM was explored numerically. Although the manufacturing process of the C-PCM could introduce unwanted defects, such as porosities, superficial asperities or non-perfect thermal contacts at the interface between the PCM and the metallic domain, that could modify the C-PCM thermal response, the trends observed in this study through the numerical simulations are still valid.

Lattices of different cell sizes and porosity made of Al-Si7-Mg0.4 alloy were considered. The thermal response of C-PCM containing PS lattice was compared to conventional metallic foams, here mimicked as an inverse BCC structure, in relation to their design parameters. The results of the study can be summarised as follows:

- The geometrical parameters related to the C-PCM design were analytically formalised as porosity-dependent size-normalised equations. They represent a simple tool for identifying Al-alloy lattices' manufacturability via AM techniques, checking the possibility of being filled with molten paraffinic PCM and the C-PCM performances (i.e., surface-to-volume ratios).
- Steady-state Finite Element Analyses were addressed to estimate phase arrangement-dependent thermal conductivity. The effective thermal conductivity of the PS-based C-PCM resulted in being 68 % of the maximum achievable value in the porosity range of 0.8–0.99.
- Transient analyses demonstrate that PS is advantageous over BCC for faster responses at fixed porosity due to the higher thermal conductivity, higher PCM surface-to-volume ratio and smaller diameters of the sphere inscribed in the void domains.
- Porosity-dependence analyses on PS-based C-PCMs highlighted the possibility of increasing the storage potential and the porosity. However, at the same time, an increment in the C-PCM porosity corresponds to latent heat slower storage process and more pronounced temperature inhomogeneities in the PCM caused by lower thermal conductivity and higher sphere diameters.
- Smaller cell sizes (i.e., smaller sphere diameters) grantee slightly faster transients at fixed porosity. The relative changes in the melting time with respect to the lattice size become wider as the heating rate increases.
- The feasibility of designing a 3-phase composite with two PCMs having different transient ranges was demonstrated. During heating, the phase transition of the low-temperature PCM causes temperature difference and thermal interaction with the high-melting PCM. The inverse situation occurs as the high-melting PCM melts. The potential use of a 3-phase C-PCM for developing thermal management devices is demonstrated. The discussion also has highlighted the possibility of using this 3-phase system to tune the temperature of a device coupled to it within the melting range of the two PCMs.

CRediT authorship contribution statement

Matteo Molteni: Investigation, Visualization, Writing – original draft, Writing – review & editing. **Sara Candidori:** Investigation, Visualization, Writing – review & editing. **Serena Graziosi:** Conceptualization, Methodology, Validation, Writing – review & editing. **Elisabetta Gariboldi:** Conceptualization, Methodology, Validation, Writing – review & editing.

Declaration of competing interest

The authors declare that they have no known competing financial interests or personal relationships that could have appeared to influence the work reported in this paper.

Data availability

The raw data required to reproduce these findings cannot be shared at this time as the data also forms part of an ongoing study. The processed data required to reproduce these findings cannot be shared at this time as the data also forms part of an ongoing study.

Acknowledgements

The authors acknowledge the partial support by the Italian Ministry of Education, University and Research through the PhD grant "Multifunctional Metallic and Hybrid Materials", funded on ESF-REACT EU sources (Ministerial Decreet 1061/2021) from the National Operational Plan "Research and Innovation" 2014-2020 – Action IV.5 (PhD on Green Technologies).

References

[1] S. Ahmadi, A.H. Fakehi, A. Vakili, M. Moeini-Aghtaie, An optimization model for the long-term energy planning based on useful energy, economic and environmental pollution reduction in residential sector: a case of Iran, J. Build. Eng. 30 (2020), 101247, https://doi.org/10.1016/j.jobe.2020.101247.
[2] J.K. Mwangi, W.J. Lee, Y.C. Chang, C.Y. Chen, L.C. Wang, An overview: energy saving and pollution reduction by using green fuel blends in diesel engines, Appl. Energy 159 (2015) 214–236, https://doi.org/10.1016/j.apenergy.2015.08.084.
[3] J. Klemeš, S. Pierucci, E. Worrell, Sustainable processes thorough LCA, process integration and optimal design, Resour. Conserv. Recycl. 50 (2007) 115–121, https://doi.org/10.1016/j.resconrec.2006.06.010.
[4] I. Sarbu, A. Dorca, Review on heat transfer analysis in thermal energy storage using latent heat storage systems and phase change materials, Int. J. Energy Res. 43 (2019) 29–64, https://doi.org/10.1002/er.4196.
[5] P.H. Feng, B.C. Zhao, R.Z. Wang, Thermophysical heat storage for cooling, heating, and power generation: a review, Appl. Therm. Eng. 166 (2020), 114728, https://doi.org/10.1016/j.applthermaleng.2019.114728.
[6] A. Sharma, V.V. Tyagi, C.R. Chen, D. Buddhi, Review on thermal energy storage with phase change materials and applications, Renew. Sust. Energ. Rev. 13 (2009) 318–345, https://doi.org/10.1016/j.rser.2007.10.005.
[7] K. Pielichowska, K. Pielichowski, Phase change materials for thermal energy storage, Prog. Mater. Sci. 65 (2014) 67–123, https://doi.org/10.1016/j.pmatsci.2014.03.005.
[8] M. Aramesh, B. Shabani, Metal foams application to enhance the thermal performance of phase change materials: a review of experimental studies to understand the mechanisms, J. Energy Storage 50 (2022), 104650, https://doi.org/10.1016/j.est.2022.104650.
[9] C.Y. Zhao, W. Lu, Y. Tian, Heat transfer enhancement for thermal energy storage using metal foams embedded within phase change materials (PCMs), Sol. Energy 84 (2010) 1402–1412, https://doi.org/10.1016/j.solener.2010.04.022.

[10] X. Tong, N. Li, M. Zeng, Q. Wang, Organic phase change materials confined in carbon-based materials for thermal properties enhancement: recent advancement and challenges, Renew. Sust. Energ. Rev. 108 (2019) 398–422, https://doi.org/10.1016/j.rser.2019.03.031.

[11] M. Maleki, H. Karimian, M. Shokouhimehr, R. Ahmadi, A. Valanezhad, A. Beitollahi, Development of graphitic domains in carbon foams for high efficient electro/photo-to-thermal energy conversion phase change composites, Chem. Eng. J. 362 (2019) 469–481, https://doi.org/10.1016/j.cej.2019.01.032.

[12] G. Gedler, M. Antunes, T. Borca-Tasciuc, J.I. Velasco, R. Ozisik, Effects of graphene concentration, relative density and cellular morphology on the thermal conductivity of polycarbonate-graphene nanocomposite foams, Eur. Polym. J. 75 (2016) 190–199, https://doi.org/10.1016/j.eurpolymj.2015.12.018.

[13] J.L. Zeng, F.R. Zhu, S.B. Yu, L. Zhu, Z. Cao, L.X. Sun, G.R. Deng, W.P. Yan, L. Zhang, Effects of copper nanowires on the properties of an organic phase change material, Sol. Energy Mater. Sol. Cells 105 (2012) 174–178, https://doi.org/10.1016/j.solmat.2012.06.013.

[14] J.L. Zeng, Z. Cao, D.W. Yang, L.X. Sun, L. Zhang, Thermal conductivity enhancement of Ag nanowires on an organic phase change material, J. Therm. Anal. Calorim. 101 (2010) 385–389, https://doi.org/10.1007/s10973-009-0472-y.

[15] K. Pietrak, T.S. Wi, A Review of Models for Effective Thermal Conductivity of Composite Materials 95, 2015, pp. 14–24.

[16] B. Vayre, F. Vignat, F. Villeneuve, Designing for additive manufacturing, Procedia CIRP 3 (2012) 632–637, https://doi.org/10.1016/j.procir.2012.07.108.

[17] O. Diegel, A. Nordin, D. Motte, Additive Manufacturing Technologies, 2019, pp. 19–39, https://doi.org/10.1007/978-981-13-8281-9_2.

[18] S. Catchpole-Smith, R.R.J. Sélo, A.W. Davis, I.A. Ashcroft, C.J. Tuck, A. Clare, Thermal conductivity of TPMS lattice structures manufactured via laser powder bed fusion, Addit. Manuf. 30 (2019), 100846, https://doi.org/10.1016/j.addma.2019.100846.

[19] R.R.J. Sélo, S. Catchpole-Smith, I. Maskery, I. Ashcroft, C. Tuck, On the thermal conductivity of AlSi10Mg and lattice structures made by laser powder bed fusion, Addit. Manuf. 34 (2020), 101214, https://doi.org/10.1016/j.addma.2020.101214.

[20] W. Li, G. Yu, Z. Yu, Bioinspired heat exchangers based on triply periodic minimal surfaces for supercritical CO2 cycles, Appl. Therm. Eng. 179 (2020), 115686, https://doi.org/10.1016/j.applthermaleng.2020.115686.

[21] I. Kuar, P. Singh, Flow and thermal transport characteristics of triply-periodic minimal surface (TPMS)-based gyroid and Schwarz-P cellular materials.pdf, Numer. Heat Transf. Part A Appl. 79 (2021) 553–569.

[22] O. Al-Ketan, R.K. Abu Al-Rub, Multifunctional mechanical metamaterials based on triply periodic minimal surface lattices, Adv. Eng. Mater. 21 (2019), https://doi.org/10.1002/adem.201900524.

[23] O. Al-Ketan, M. Ali, M. Khalil, R. Rowshan, K.A. Khan, R.K. Abu Al-Rub, Forced convection computational fluid dynamics analysis of architected and three-dimensional printable heat sinks based on triply periodic minimal surfaces, J. Therm. Sci. Eng. Appl. 13 (2021) 1–14, https://doi.org/10.1115/1.4047385.

[24] O. Al-Ketan, R. Rowshan, R.K. Abu Al-Rub, Topology-mechanical property relationship of 3D printed strut, skeletal, and sheet based periodic metallic cellular materials, Addit. Manuf. 19 (2018) 167–183, https://doi.org/10.1016/j.addma.2017.12.006.

[25] J. Pérez, A new golden age of minimal surfaces, Not. Am. Math. Soc. 64 (2017) 347–358, https://doi.org/10.1090/noti1500.

[26] O. Al-Ketan, R.K. Abu Al-Rub, Multifunctional mechanical metamaterials based on triply periodic minimal surface lattices, Adv. Eng. Mater. 21 (2019) 1–39, https://doi.org/10.1002/adem.201900524.

[27] S. Rajagopalan, R.A. Robb, Schwarz meets Schwann: design and fabrication of biomorphic and durataxic tissue engineering scaffolds, Med. Image Anal. 10 (2006) 693–712, https://doi.org/10.1016/j.media.2006.06.001.

[28] F.P.W. Melchels, A.M.C. Barradas, C.A. Van Blitterswijk, J. De Boer, J. Feijen, D. W. Grijpma, Effects of the architecture of tissue engineering scaffolds on cell seeding and culturing, Acta Biomater. 6 (2010) 4208–4217, https://doi.org/10.1016/j.actbio.2010.06.012.

[29] L. Wang, J. Lau, E.L. Thomas, M.C. Boyce, Co-continuous composite materials for stiffness, strength, and energy dissipation, Adv. Mater. 23 (2011) 1524–1529, https://doi.org/10.1002/adma.201003956.

[30] O. Al-Ketan, A. Soliman, A.M. AlQubaisi, R.K. Abu Al-Rub, Nature-inspired lightweight cellular co-continuous composites with architected periodic gyroidal structures, Adv. Eng. Mater. 20 (2018) 1–9, https://doi.org/10.1002/adem.201700549.

[31] O. Elliott, S. Gray, M. McClay, B. Nassief, A. Nunnelley, E. Vogt, J. Ekong, K. Kardel, A. Khoshkhoo, G. Proaño, D.M. Blersch, A.L. Carrano, Design and manufacturing of high surface area 3D-printed media for moving bed bioreactors for wastewater treatment, J. Contemp. Water Res. Educ. 160 (2017) 144–156, https://doi.org/10.1111/j.1936-704x.2017.03246.x.

[32] S. Vijayavenkataraman, L. Zhang, S. Zhang, J.Y.H. Fuh, W.F. Lu, Triply periodic minimal surfaces sheet scaffolds for tissue engineering applications: an optimization approach toward biomimetic scaffold design, ACS Appl. Bio Mater. 1 (2018) 259–269, https://doi.org/10.1021/acsabm.8b00052.

[33] S.C. Kapfer, S.T. Hyde, K. Mecke, C.H. Arns, G.E. Schröder-Turk, Minimal surface scaffold designs for tissue engineering, Biomaterials 32 (2011) 6875–6882, https://doi.org/10.1016/j.biomaterials.2011.06.012.

[34] I. Maskery, L. Sturm, A.O. Aremu, A. Panesar, C.B. Williams, C.J. Tuck, R. D. Wildman, I.A. Ashcroft, R.J.M. Hague, Insights into the mechanical properties of several triply periodic minimal surface lattice structures made by polymer additive manufacturing, Polymer (Guildf.) 152 (2018) 62–71, https://doi.org/10.1016/j.polymer.2017.11.049.

[35] C. Yan, L. Hao, A. Hussein, S.L. Bubb, P. Young, D. Raymont, Evaluation of light-weight AlSi10Mg periodic cellular lattice structures fabricated via direct metal laser sintering, J. Mater. Process. Technol. 214 (2014) 856–864, https://doi.org/10.1016/j.jmatprotec.2013.12.004.

[36] I. Maskery, N.T. Aboulkhair, A.O. Aremu, C.J. Tuck, I.A. Ashcroft, Compressive failure modes and energy absorption in additively manufactured double gyroid lattices, Addit. Manuf. 16 (2017) 24–29, https://doi.org/10.1016/j.addma.2017.04.003.

[37] S.C. Han, K. Kang, Another stretching-dominated micro-architectured material, shellular, Mater. Today 31 (2019) 31–38, https://doi.org/10.1016/j.mattod.2019.05.018.

[38] M. Speirs, B. Van Hooreweder, J. Van Humbeeck, J.P. Kruth, Fatigue behaviour of NiTi shape memory alloy scaffolds produced by SLM, a unit cell design comparison, J. Mech. Behav. Biomed. Mater. 70 (2017) 53–59, https://doi.org/10.1016/j.jmbbm.2017.01.016.

[39] L. Yang, C. Yan, W. Cao, Z. Liu, B. Song, S. Wen, C. Zhang, Y. Shi, S. Yang, Compression–compression fatigue behaviour of gyroid-type triply periodic minimal surface porous structures fabricated by selective laser melting, Acta Mater. 181 (2019) 49–66, https://doi.org/10.1016/j.actamat.2019.09.042.

[40] M. Afshar, A.P. Anaraki, H. Montazerian, J. Kadkhodapour, Additive manufacturing and mechanical characterization of graded porosity scaffolds designed based on triply periodic minimal surface architectures, J. Mech. Behav. Biomed. Mater. 62 (2016) 481–494, https://doi.org/10.1016/j.jmbbm.2016.05.027.

[41] L. Yang, R. Mertens, M. Ferrucci, C. Yan, Y. Shi, S. Yang, Continuous graded Gyroid cellular structures fabricated by selective laser melting: design, manufacturing and mechanical properties, Mater. Des. 162 (2019) 394–404, https://doi.org/10.1016/j.matdes.2018.12.007.

[42] G.L. Vignoles, D. Rochais, S. Chupin, Computation of the conducto-radiative effective heat conductivity of porous media defined by triply periodic minimal surfaces, Int. J. Therm. Sci. 159 (2021), 106598, https://doi.org/10.1016/j.ijthermalsci.2020.106598.

[43] J. Feng, J. Fu, X. Yao, Y. He, Triply periodic minimal surface (TPMS) porous structures: from multi-scale design, precise additive manufacturing to multidisciplinary applications, Int. J. Extrem. Manuf. 4 (2022), https://doi.org/10.1088/2631-7990/ac5be6.

[44] H. Hu, X. Ding, L. Wang, Numerical analysis of heat transfer during multi-layer selective laser melting of AlSi10Mg, Optik (Stuttg.) 127 (2016) 8883–8891, https://doi.org/10.1016/j.ijleo.2016.06.115.

[45] S.N. Khaderi, V.S. Deshpande, N.A. Fleck, The stiffness and strength of the gyroid lattice, Int. J. Solids Struct. 51 (2014) 3866–3877, https://doi.org/10.1016/j.ijsolstr.2014.06.024.

[46] S. Torquato, A. Donev, Minimal surfaces and multifunctionality, Proc. R. Soc. A Math. Phys. Eng. Sci. 460 (2004) 1849–1856, https://doi.org/10.1098/rspa.2003.1269.

[47] S. Torquato, S. Hyun, A. Donev, Multifunctional composites: optimizing microstructures for simultaneous transport of heat and electricity, Phys. Rev. Lett. 89 (2002) 1–4, https://doi.org/10.1103/PhysRevLett.89.266601.

[48] H. Karcher, K. Polthier, Construction of triply periodic minimal surfaces, Philos. Trans. R. Soc. Lond. A 354 (1996) 2077–2104.

[49] E.A. Lord, A.L. Mackay, Periodic minimal surfaces of cubic symmetry, Curr. Sci. 85 (2003) 346–362.

[50] O. Al-Ketan, R.K. Abu Al-Rub, MSLattice: a free software for generating uniform and graded lattices based on triply periodic minimal surfaces, Mater. Des. Process. Commun. 3 (2021) 1–10, https://doi.org/10.1002/mdp2.205.

[51] K. Lafdi, O. Mesalhy, S. Shaikh, Experimental study on the influence of foam porosity and pore size on the melting of phase change materials, J. Appl. Phys. 102 (2007), https://doi.org/10.1063/1.2802183.

[52] E. Gariboldi, L.P.M. Colombo, D. Fagiani, Z. Li, Methods to characterize effective thermal conductivity, diffusivity and thermal response in change materials, Materials (Basel) 12 (2019) 1–23.

[53] S. Piacquadio, M. Schirp-Schoenen, M. Mameli, S. Filippeschi, K.U. Schröder, Experimental analysis of the thermal energy storage potential of a phase change material embedded in additively manufactured lattice structures, Appl. Therm. Eng. 216 (2022), https://doi.org/10.1016/j.applthermaleng.2022.119091.

[54] C. Hu, H. Li, D. Tang, J. Zhu, K. Wang, X. Hu, M. Bai, Pore-scale investigation on the heat-storage characteristics of phase change material in graded copper foam, Appl. Therm. Eng. 178 (2020), 115609, https://doi.org/10.1016/j.applthermaleng.2020.115609.

[55] Z. Li, E. Gariboldi, Modelling the conditions for natural convection onset in open-cell porous Al/paraffin composite phase change materials: effects of temperature, paraffin type and metallic structure geometry, Int. J. Heat Mass Transf. 173 (2021), 121279, https://doi.org/10.1016/j.ijheatmasstransfer.2021.121279.

[56] S.V. Garimella, Direct Simulation of Transport in Open-Cell Metal Foam 128, 2006, pp. 793–799, https://doi.org/10.1115/1.2227038.

[57] I. Ngo, C. Byon, Permeability of microporous wicks with geometric inverse to sintered particles, Int. J. Heat Mass Transf. 92 (2016) 298–302, https://doi.org/10.1016/j.ijheatmasstransfer.2015.08.040.

[58] Z.A. Qureshi, S.A.B. Al-Omari, E. Elnajjar, O. Al-Ketan, R.A. Al-Rub, Using triply periodic minimal surfaces (TPMS)-based metal foams structures as skeleton for metal-foam-PCM composites for thermal energy storage and energy management applications, Int. Commun. Heat Mass Transf. 124 (2021), 105265, https://doi.org/10.1016/j.icheatmasstransfer.2021.105265.

[59] Z.A. Qureshi, S.A.B. Al-Omari, E. Elnajjar, O. Al-Ketan, R. Abu Al-Rub, Nature-inspired triply periodic minimal surface-based structures in sheet and solid configurations for performance enhancement of a low-thermal-conductivity phase-change material for latent-heat thermal-energy-storage applications, Int. J. Therm. Sci. 173 (2022), 107361, https://doi.org/10.1016/j.ijthermalsci.2021.107361.
[60] Z.A. Qureshi, S.A.B. Al Omari, E. Elnajjar, F. Mahmoud, O. Al-Ketan, R.A. Al-Rub, Thermal characterization of 3D-printed lattices based on triply periodic minimal surfaces embedded with organic phase change material, Case Stud. Therm. Eng. 27 (2021), 101315, https://doi.org/10.1016/j.csite.2021.101315.
[61] Z.A. Qureshi, S. Addin Burhan Al-Omari, E. Elnajjar, O. Al-Ketan, R.A. Al-Rub, On the effect of porosity and functional grading of 3D printable triply periodic minimal surface (TPMS) based architected lattices embedded with a phase change material, Int. J. Heat Mass Transf. 183 (2022), 122111, https://doi.org/10.1016/j.ijheatmasstransfer.2021.122111.
[62] Z.A. Qureshi, E. Elnajjar, O. Al-Ketan, R.A. Al-Rub, S.B. Al-Omari, Heat transfer performance of a finned metal foam-phase change material (FMF-PCM) system incorporating triply periodic minimal surfaces (TPMS), Int. J. Heat Mass Transf. 170 (2021), https://doi.org/10.1016/j.ijheatmasstransfer.2021.121001.
[63] Z. Li, E. Gariboldi, Review on the temperature-dependent thermophysical properties of liquid paraffins and composite phase change materials with metallic porous structures, Mater. Today Energy 20 (2021), https://doi.org/10.1016/j.mtener.2021.100642.
[64] H. Zheng, C. Wang, Q. Liu, Z. Tian, X. Fan, Thermal performance of copper foam/paraffin composite phase change material, Energy Convers. Manag. 157 (2018) 372–381, https://doi.org/10.1016/j.enconman.2017.12.023.
[65] Q. Jiang, P. Zhang, Z. Yu, H. Shi, D. Wu, H. Yan, X. Ye, Q. Lu, Y. Tian, A review on additive manufacturing of pure copper, Coatings 11 (2021), https://doi.org/10.3390/coatings11060740.
[66] Z. Li, E. Gariboldi, On the use of effective thermophysical properties to predict the melting process of composite phase change materials with coarse structures, Int. J. Heat Mass Transf. 180 (2021), 121765, https://doi.org/10.1016/j.ijheatmasstransfer.2021.121765.
[67] W. Xu, H. Zhang, Z. Yang, J. Zhang, The effective thermal conductivity of three-dimensional reticulated foam materials, J. Porous. Mater. 16 (2009) 65–71, https://doi.org/10.1007/s10934-007-9169-4.
[68] C. Bonatti, D. Mohr, Smooth-shell metamaterials of cubic symmetry: anisotropic elasticity, yield strength and specific energy absorption, Acta Mater. 164 (2019) 301–321, https://doi.org/10.1016/j.actamat.2018.10.034.
[69] T. Poltue, C. Karuna, S. Khrueaduangkham, S. Seehanam, P. Promoppatum, Design exploration of 3D-printed triply periodic minimal surface scaffolds for bone implants, Int. J. Mech. Sci. 211 (2021), 106762, https://doi.org/10.1016/j.ijmecsci.2021.106762.
[70] D.W. Abueidda, A.S. Dalaq, R.K. Abu Al-Rub, H.A. Younes, Finite element predictions of effective multifunctional properties of interpenetrating phase composites with novel triply periodic solid shell architectured reinforcements, Int. J. Mech. Sci. 92 (2015) 80–89, https://doi.org/10.1016/j.ijmecsci.2014.12.004.
[71] Y. Lu, L.L. Cheng, Z. Yang, J. Li, H. Zhu, Relationship between the morphological, mechanical and permeability properties of porous bone scaffolds and the underlying microstructure, PLoS One 15 (2020) 1–19, https://doi.org/10.1371/journal.pone.0238471.
[72] J.Y. Ho, K.C. Leong, T.N. Wong, Experimental and numerical investigation of forced convection heat transfer in porous lattice structures produced by selective laser melting, Int. J. Therm. Sci. 137 (2019) 276–287, https://doi.org/10.1016/j.ijthermalsci.2018.11.022.
[73] B. Lotfi, B.A. Sunden, A novel trussed fin-and-elliptical tube heat exchanger with periodic cellular lattice structures, Int. J. Numer. Methods Heat Fluid Flow (2022), https://doi.org/10.1108/HFF-04-2022-0206.
[74] T. Dixit, E. Al-Hajri, M.C. Paul, P. Nithiarasu, S. Kumar, High performance, microarchitected, compact heat exchanger enabled by 3D printing, Appl. Therm. Eng. 210 (2022), 118339, https://doi.org/10.1016/j.applthermaleng.2022.118339.
[75] R.A. Overfelt, S.I. Bakhtiyarov, R.E. Taylor, Thermophysical properties of A201, A319, and A356 aluminium casting alloys, High Temp. - High Press. 34 (2002) 401–409, https://doi.org/10.1068/htjr052.
[76] S.I. Bakhtiyarov, R.A. Overfelt, S.G. Teodorescu, Electrical and thermal conductivity of A319 and A356 aluminum alloys, J. Mater. Sci. 36 (2001) 4643–4648, https://doi.org/10.1023/A:1017946130966.
[77] S.W. Kim, K. Park, S.H. Lee, K.H. Kang, K.T. Lim, Thermophysical properties of automotive metallic brake disk materials, Int. J. Thermophys. 29 (2008) 2179–2188, https://doi.org/10.1007/s10765-008-0537-3.
[78] S. Roy, L.F. Allard, A. Rodriguez, W.D. Porter, A. Shyam, Comparative evaluation of cast aluminum alloys for automotive cylinder heads: part II—mechanical and thermal properties, Metall. Mater. Trans. A Phys. Metall. Mater. Sci. 48 (2017) 2543–2562, https://doi.org/10.1007/s11661-017-3986-0.
[79] R. Casati, M. Coduri, S. Checchia, M. Vedani, Insight into the effect of different thermal treatment routes on the microstructure of AlSi7Mg produced by laser powder bed fusion, Mater. Charact. 172 (2021), 110881, https://doi.org/10.1016/j.matchar.2021.110881.
[80] G.S. Parks, G.E. Moore, M.L. Renquist, B.F. Naylor, L.A. McClaine, P.S. Fujii, J. A. Hatton, Thermal data on organic compounds. XXV. Some heat capacity, entropy and free energy data for nine hydrocarbons of high molecular weight, J. Am. Chem. Soc. 71 (1949) 3386–3389, https://doi.org/10.1021/ja01178a034.
[81] M.E. Spaght, T.S. Benson, G.S. Parks, Some heat-capacity data on organic compounds, obtained with a radiation calorimeter, J. Phys. Chem. 36 (1932) 882–888.
[82] F.P. Fleming, L. de Andrade Silva, G. dos S.V. Lima, I. Herzog, H.R.B. Orlande, J. L. Daridon, J. Pauly, L.F.A. Azevedo, Thermal conductivity of heavy, even-carbon number n-alkanes (C22 to C32), Fluid Phase Equilib. 477 (2018) 78–86, https://doi.org/10.1016/j.fluid.2018.08.016.
[83] G.A. Lane, Low temperature heat storage with phase change materials, Int. J. Ambient Energy 1 (1980) 155–168, https://doi.org/10.1080/01430750.1980.9675731.
[84] J. Gasia, J. Diriken, M. Bourke, J. Van Bael, L.F. Cabeza, Comparative study of the thermal performance of four different shell-and-tube heat exchangers used as latent heat thermal energy storage systems, Renew. Energy 114 (2017) 934–944, https://doi.org/10.1016/j.renene.2017.07.114.
[85] N. Ukrainczyk, S. Kurajica, J. Šipušić, Thermophysical comparison of five commercial paraffin waxes as latent heat storage materials, Chem. Biochem. Eng. Q. 24 (2010) 129–137.
[86] M. Usman, F. Siddiqui, A. Ehsan, R.A. Sadaqat, A. Hussain, Improvement of thermal conductivity of paraffin wax, a phase change material with graphite powder, in: Proc. 2020 17th Int. Bhurban Conf. Appl. Sci. Technol. IBCAST 2020, 2020, pp. 16–25, https://doi.org/10.1109/IBCAST47879.2020.9044541.
[87] B. Buonomo, H. Celik, D. Ercole, O. Manca, M. Mobedi, Numerical study on latent thermal energy storage systems with aluminum foam in local thermal equilibrium, Appl. Therm. Eng. 159 (2019), 113980, https://doi.org/10.1016/j.applthermaleng.2019.113980.
[88] J.L. Song, Q.G. Guo, Y.J. Zhong, X.Q. Gao, Z.H. Feng, Z. Fan, J.L. Shi, L. Liu, Thermophysical properties of high-density graphite foams and their paraffin composites, Xinxing Tan Cailiao/New Carbon Mater. 27 (2012) 27–34, https://doi.org/10.1016/S1872-5805(12)60002-X.
[89] Y. Tian, C.Y. Zhao, A numerical investigation of heat transfer in phase change materials (PCMs) embedded in porous metals, Energy 36 (2011) 5539–5546, https://doi.org/10.1016/j.energy.2011.07.019.
[90] H. Zheng, C. Wang, Q. Liu, Z. Tian, X. Fan, Thermal performance of copper foam/paraffin composite phase change material, Energy Convers. Manag. 157 (2018) 372–381, https://doi.org/10.1016/j.enconman.2017.12.023.
[91] C. Vélez, M. Khayet, J.M. Ortiz De Zárate, Temperature-dependent thermal properties of solid/liquid phase change even-numbered n-alkanes: N-hexadecane, n-octadecane and n-eicosane, Appl. Energy 143 (2015) 383–394, https://doi.org/10.1016/j.apenergy.2015.01.054.
[92] G. Raza, Y. Shi, Y. Deng, Expanded graphite as thermal conductivity enhancer for paraffin wax being used in thermal energy storage systems, in: Proc. 2016 13th Int. Bhurban Conf. Appl. Sci. Technol. IBCAST 2016, 2016, pp. 1–12, https://doi.org/10.1109/IBCAST.2016.7429846.
[93] M. Kenisarin, K. Mahkamov, F. Kahwash, I. Makhkamova, Enhancing thermal conductivity of paraffin wax 53–57 °C using expanded graphite, Sol. Energy Mater. Sol. Cells 200 (2019), 110026, https://doi.org/10.1016/j.solmat.2019.110026.
[94] F.P. Incropera, D.P. DeWitt, Fundamentals of Heat and Mass Transfer, 1996, p. 890, https://doi.org/10.1016/j.applthermaleng.2011.03.022.
[95] E. Gariboldi, Z. Li, A.J. Rawson, Effective thermal conductivity in BCC and FCC lattices for all volume fractions and conductivity ratios: analyses by microstructural efficiency and morphology factor and analytic models, Mater. Today Commun. 33 (2022), 104253, https://doi.org/10.1016/j.mtcomm.2022.104253.
[96] N. Kladovasilakis, K. Tsongas, I. Kostavelis, D. Tzovaras, D. Tzetzis, Effective mechanical properties of additive manufactured triply periodic minimal surfaces: experimental and finite element study, Int. J. Adv. Manuf. Technol. 121 (2022) 7169–7189, https://doi.org/10.1007/s00170-022-09651-w.
[97] C.J. Ejeh, I. Barsoum, R.K. Abu Al-Rub, Flexural properties of functionally graded additively manufactured AlSi10Mg TPMS latticed-beams, Int. J. Mech. Sci. 223 (2022), 107293, https://doi.org/10.1016/j.ijmecsci.2022.107293.
[98] J. Zhu, S. Zou, Y. Mu, J. Wang, Y. Jin, Additively Manufactured Scaffolds With Optimized Thickness Based on Triply Periodic Minimal Surface, 2022.
[99] A. Baroutaji, A. Arjunan, J. Beal, J. Robinson, J. Coroado, The influence of atmospheric oxygen content on the mechanical properties of selectively laser melted AlSi10Mg, Materials (Basel) 430 (2023) 1–14.
[100] M. Subramanian, A.T. Hoang, K. B, S. Nižetić, J.M. Solomon, D. Balasubramanian, S. C, T. G, H. Metghalchi, X.P. Nguyen, A technical review on composite phase change material based secondary assisted battery thermal management system for electric vehicles, J. Clean. Prod. 322 (2021), https://doi.org/10.1016/j.jclepro.2021.129079.
[101] R. Stropnik, U. Stritih, Increasing the efficiency of PV panel with the use of PCM, Renew. Energy 97 (2016) 671–679, https://doi.org/10.1016/j.renene.2016.06.011.
[102] T.M. Tritt, Thermoelectric materials: principles, structure, properties, and applications, in: Encycl. Mater. Sci. Technol, 2002, pp. 1–11, https://doi.org/10.1016/b0-08-043152-6/01822-2.